UNIVERSITY OF OKLAHOMA
GRADUATE COLLEGE

AN EXAMINATION OF THE BEHAVIOR OF A GIANT HAIL-PRODUCING SUPERCELL IN OKLAHOMA ON 23 MAY 2011 USING DATA FROM FIVE DOPPLER RADARS

A THESIS
SUBMITTED TO THE GRADUATE FACULTY
in partial fulfillment of the requirements for the
Degree of
MASTER OF SCIENCE

By
LEAH M. SWINNEY
Norman, Oklahoma
2024

AN EXAMINATION OF THE BEHAVIOR OF A GIANT HAIL-PRODUCING SUPERCELL IN OKLAHOMA ON 23 MAY 2011 USING DATA FROM FIVE DOPPLER RADARS

A THESIS APPROVED FOR THE
SCHOOL OF METEOROLOGY

BY THE COMMITTEE CONSISTING OF

Dr. Howard B. Bluestein, Chair

Dr. Jeffrey C. Snyder

Dr. David Bodine

Acknowledgments

I want to express my gratitude to the people who have played a significant role in my life and have helped me get to where I am today. Firstly, I want to thank my mom for her unwavering support throughout my life. Thank you for sparking my interest in meteorology with a toy weather kit. Your support and encouragement have been so crucial in shaping my educational journey. I want to thank my grandparents for instilling in me a love for animals and plants. To the rest of my family, thank you for always believing in me and supporting me. To my family: Cuando me vean volar, recuerden: ustedes me pintaron las alas.

I want to give a special thank you to my boyfriend, Connor, for always being there when I needed it the most. Your support has made grad school less stressful and has always motivated me to pursue my goals. I would also like to thank my friends, Theresa, Emily, Owen, Tyler, and many others, for making my life outside of grad school enjoyable. A heartfelt thank you to my pets - Tesla, Torti, Mango, and Rue - for being the best support animals I can ask for and for providing endless cuddles.

I am deeply grateful to my advisor, Dr. Howie Bluestein, for his invaluable guidance and support throughout my research. Our research meetings, discussions, and travels in RaXPol have been enriching, providing me with both knowledge and memorable experiences. Thank you, Dr. Bluestein, for your patience and encouragement and for giving me the opportunity to pursue and achieve my academic goals. I would also like to thank my committee members, Dr. Jeff Snyder and Dr. David Bodine, for being part of my committee and for their help in this process. I appreciate our discussions and their constructive feedback, which helped significantly improve this thesis. I would also like to express my gratitude to the LROSE team, Dr. Jennifer DeHart, and

Dr. Michael Bell, who provided help and feedback with the LROSE software and troubleshooting problems that arose.

Lastly, I would like to thank CIRWO for selecting me as the second recipient of the Research to Transform Diversity Graduate Assistantship. This has been a wonderful experience, and I am excited to see this assistantship grow. This work was funded by the Research to Transform Diversity Graduate Assistantship with CIWRO, the Cooperative Institute of Weather Research Operations. The RaXPol data collection presented in this project was supported through NSF MRI grant AGS-0821231 and NSF grants AGS-0934307 and AGS-1947146 awarded to the University of Oklahoma.

Table of Contents

List of Tables

List of Figures

Abstract

Dual-polarization radar observations are valuable for identifying the location and evolution of hail in supercells. This study presents an analysis of a supercell that produced remarkably large hail [6 inches (15.24 cm) in diameter, setting a state record for Oklahoma at the time] on 23 May 2011 in the southwestern part of the state. This analysis uses data from three X-band, ground-based, mobile Doppler radars – RaXPol, MWR-05XP, and NOXP – each positioned generally to the southeast of the storm's updraft in close proximity to each other, in addition to observations from two WSR-88Ds, KFDR located in Frederick, Oklahoma and KOUN located in Norman, Oklahoma. Of the five radars, all but the MWR-05XP and KFDR had polarimetric capabilities; the MWR-05XP, however, had rapid-scan, hybrid, phased-array technology.

The investigation provides an in-depth examination of the storm's evolution, combining data analyses from all three mobile radars and the two stationary WSR-88D radars. The results of polarimetric variable comparisons, multi-Doppler wind analyses, and dual-frequency analyses will be presented. The main goal of this study is to contribute to an improved understanding of the transformation of hydrometeors, particularly hail, from their initial generation within the updraft to their eventual descent to the ground in a historic storm. A secondary goal is to document a failed attempt at tornadogenesis which was associated with a funnel cloud and examine why a tornado did not form.

Chapter 1

Introduction

Severe storms that produce large hail pose a threat to structures, property, and agriculture. In the United States, hailstorms have resulted in more than $10 billion in losses annually (Gunturi & Tippett. 2017; Allen et al. 2020; Faust et al. 2022). The impacts of these hailstorms are felt locally and globally, affecting businesses, homeowners, and more. The economic consequences of hailstorms motivate the importance of gaining a deeper understanding of the processes involved in hailstone formation and the evolution of the storms that produce them.

Previous field experiments focusing on hail were conducted in the 1970s and 1980s and have significantly contributed to our current understanding of hailstone formation and its evolution within storm updrafts. The National Hail Research Experiment (NHRE), conducted from 1972 to 1976, and the Cooperative Convective Precipitation Experiment (CCOPE) in 1981 are the most recent U.S hail-dedicated campaigns. Findings from the NHRE indicated that the primary hail growth regions were around the updraft edges rather than the center. CCOPE provided insights into how microphysical processes and kinematics within storms and the environment influence precipitation development. Recent field campaigns, such as the Severe Hazards Analysis and Verification Experiment (SHAVE) from 2006 to 2015, have further advanced our knowledge by increasing the verification of hail reports. The Hail Spatial and Temporal Observing Network Effort (HailSTONE), conducted from 2011 to 2015, showed that forecasted hail sizes were larger than the observed hailstone sizes from severe thunderstorms (Blair et al. 2017).

For decades, radar technology has been utilized to observe and study hailstorms. The integration of dual-polarization to the United States Weather Surveillance Radar-1988 Doppler (WSR-88D) radar network, which was completed in 2013, has significantly enhanced our understanding of the microphysical and dynamical processes of hailstorms. This addition has enabled numerous studies on polarimetric variables, their characteristics, and their differences across various types of hydrometeors (Snyder et al. 2013). Most of these studies involve the operational S-band NEXRAD radars, which offer high spatial resolution and an update time of approximately 5 minutes. Despite their ability to observe most hailstorms, these radars have limitations when it comes to observing the evolution of these storms and the growth of the hydrometeors. Collecting near-surface data is nearly impossible due to the Earth's curvature and beam blockage from topography and buildings. At greater distances, the radar beam's dispersion can result in the loss of critical storm structures (Wurman et al. 1997; Bluestein et al. 2007).

Mobile Doppler radars have been a critical tool for addressing these limitations. The concept of portable radars was first proposed by Zrnic et al. (1985) and was first realized by Bluestein and Unruh (1989). The first portable radar was low-powered, bistatic, X-band (3 cm), Doppler radar from the Los Alamos National Laboratory (LANL), originally intended for non-meteorological applications. This radar was deployed manually by setting it on a stand and pointing it storms by hand, with the data received being converted into audio signals. Despite having a 5° beamwidth, the data collected demonstrated approaching and receding velocities associated with cyclonic circulations in supercells. This early deployment demonstrated the feasibility of using portable radars to collect data in tornadic supercells.

Following the success of the initial radar field deployment, the LANL radar was deployed six more times in 1990 and 1991, where it observed winds of approximately 125 ms^{-1} associated with a tornado. The success of the LANL radar highlighted the need for a higher-resolution radar to advance supercell observations. In response, Bluestein et al. (1995) field-tested the University of Massachusetts (U-Mass) W-band (3 mm) radar in 1993 and 1994. Mounted inside a van, the U-Mass radar had a beamwidth of 0.7°, resulting in a greater spatial resolution. In subsequent years, more mobile weather radars were developed to collect data on near-surface microscale phenomena. Notable examples include the Doppler on Wheels (DOW), the first truck-mounted X-band radar (Wurman et al. 1997), the MWR-05XP a repurposed military phased array radar (Bluestein et al. 2010), and RaXPol, a rapid scan, X-band, dual-polarimetric radar (Pazmany et al. 2013). Specifications of the MWR-05XP and RaXPol are discussed in greater detail in Chapter 3.

Previous studies have examined the characteristics of hailstorms using rapid scan radar observations. Witt et al. (2018) conducted a study on the 31 May 2013 El Reno storm, which was observed by multiple radars. The analysis provided crucial insights concerning the presence and spatial distribution of giant hailstones (defined in that study as hailstones larger than 7 cm in diameter). Findings show that these giant hailstones were predominantly located outside the storm's main precipitation core, specifically in regions with moderate reflectivities between 40 to 50 dB*Z* at S band (Witt et al. 2018). Polarimetric data from KOUN and RaXPol indicated distinctive dual-polarization signatures. These signatures included low values of differential reflectivity (Z_{DR}), correlation coefficient (ρ_{HV}), and specific differential phase (K_{DP}), consistent with previous observations of large hail. Furthermore, the spatial distribution analysis revealed that the giant hailstones were concentrated northeast, and northwest of the tornado associated with the storm (Witt et al. 2018). This pattern provides valuable insights into the dynamics of hail formation and scattering within severe convective storms, contributing to our understanding of hailstorm behavior. Connecting the polarimetric signatures associated with giant hail and their locations within the supercell allows future studies to search for similar variable patterns and corresponding locations within a supercell for potential giant hailstones.

On May 23rd, 2011, a supercell formed in southwestern Oklahoma, became a prolific giant hail producer, and was observed by five radars from its formation to its eventual decay. The primary focus of this study is to analyze the collected data and compare the observations of the storm from multiple radar systems, documenting the evolution of the supercell through different perspectives. This study also aims to document a failed attempt at tornadogenesis associated with a funnel cloud. Questions that will be addressed are: 1) What can the evolution of the polarimetric variables tell us about hail development? 2) What are the similarities and differences between polarimetric variables measured by radars that scanned the storm simultaneously? Ultimately, this study aims to enhance our understanding of the transformation of hail, from initial generation within the updraft to eventual descent to the ground in an historic storm. Chapter 2 provides background information on hail microphysics, the polarimetric variables considered in this study, and the polarimetric signatures that are commonly observed in hailstorms. Chapter 3 describes the instrumentation and datasets used in this study as well as the methods for processing and analyzing the data. Chapters 4 and 5 provide a thorough examination of the hailstorm's evolution and results from analyses done on the storm. Finally, Chapter 6 provides a summary of the case study and recommends future work.

Chapter 2

Background

2.1 Hail Microphysics

2.1.1 Formation of Hailstones in Convective Storms

Hailstones develop within strong convective storms with intense updrafts, beginning with a small particle, usually less than 1 cm in diameter, that acts as the nucleus for the hail embryo (Allen et al. 2020). These embryos originate from graupel or frozen droplets (Knight and Knight 1970; Heymsfield 1982; Allen et al. 2020). However, only some storms containing these embryos produce hail that is observed at the ground; specific environmental conditions are necessary for hail development, particularly an ample amount of supercooled liquid water. Hail growth happens when these supercooled liquid water drops accumulate on the hail embryo by either riming or accretion. In riming, droplets freeze immediately upon contact, whereas in accretion, the droplets remain at least partially liquid after contacting the hailstone. The area of ample supercooled liquid droplets is called the hail growth zone (HGZ) and is typically located between -10°C and -25°C (Knight et al. 1975; Nelson 1983; Foote 1984). The time hailstones spend in the HGZ is influenced by their trajectory, which varies based on the fall speed, updraft speed, and horizontal airflow (Allen et al. 2020). Stronger and wider updrafts also tend to enhance hail growth potential (Allen et al. 2020; Dennis and Kumjian 2017; Nelson 1983). Hail embryos need approximately 10 to 15 minutes in the HGZ to develop into large hailstones (Heymsfield 1982; Nelson 1983, Foote 1984).

2.1.2 Hail Growth Processes

If conditions permit, severe convective storms can produce large hailstones. The main mechanism for hailstone growth involves the accumulation of supercooled liquid drops and raindrops within the storm's updraft. Vapor deposition can also contribute to hailstone growth, though it is less common and less significant (Nelson 1983; Rasmussen & Heymsfield 1987a). There are two main growth regimes for hailstones: dry growth and wet growth (e.g., Lamb and Verlinde 2011). In the dry growth regime, the surface temperature of the hailstone remains below 0° C, causing the accreted water droplets to freeze immediately upon contact. This regime is typically associated with smaller hailstones and occurs in regions of the storm with relatively low liquid water content. Conversely, the wet growth regime occurs when the hailstone's surface temperature rises to 0°C or higher due to latent heat release from freezing droplets. This results in a thin layer of liquid water on the hailstone's surface, allowing for the capture of more water droplets before they freeze. Hailstone growth recipes may switch between dry and wet growth during the hailstone's lifecycle, with larger hailstones often ending in the wet growth regime (Knight and Knight, 1970). The growth regimes affect the hailstone's density and influence it's shape, although there is wide variability of both nature. Most hailstones tend to be oblate spheroids, though larger hailstones are often more irregularly shaped. (Allen et al. 2020; Shedd et al. 2021).

2.1.3 Melting and Shedding

As hailstones grow, they either advect horizontally out of the updraft or their fall speed eventually exceeds the updraft speed; in either case, they descend. Upon descending, the hailstones typically enter a layer of warmer (above 0° C) air, during which melting commences. This process can result in the outer layer shedding water, reducing the size of the stone. The amount of melting

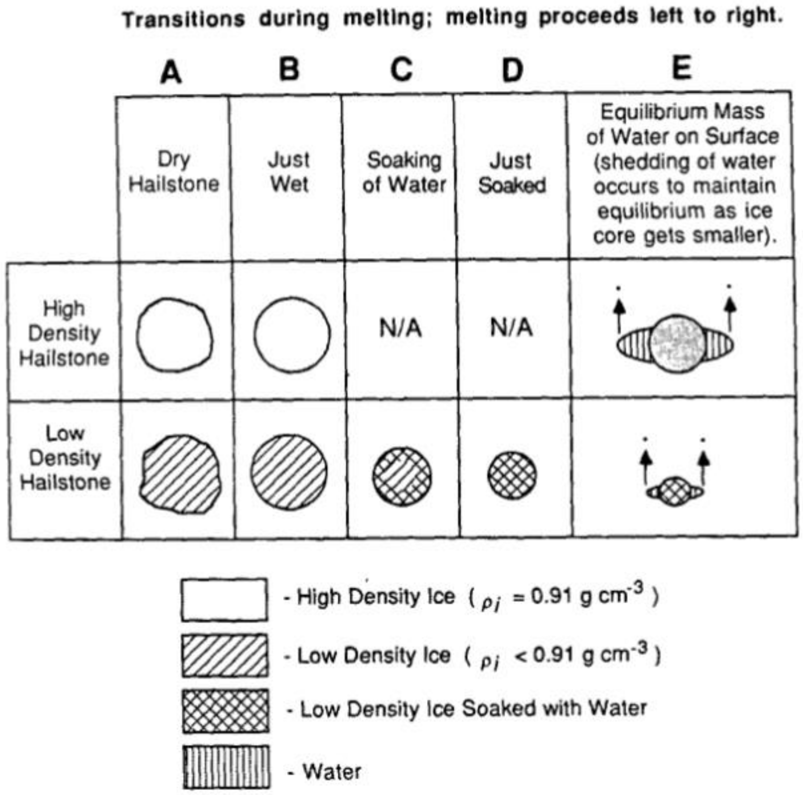

Figure 2.1: Schematic showing the stages of melting for hail. Figure 1 in Rasmussen and Heymsfield (1987a).

depends on the warm layer's thickness, magnitude, and relative humidity and on the hailstone's fall speed. The upward drag force causes this liquid to collect around the hailstone's circumference water torus, which may stabilize the orientation of the hailstone (Figure 2.1). The shedding continues until the hailstones either reach the surface or melt completely.

2.2 Radar Observations of Hailstorms

Before the adoption of dual-polarization technology, conventional (single-polarization) Doppler radars measured three key moments: radar reflectivity factor (Z), Doppler velocity (V_r), and spectrum width (W). However, these radars had limitations; using only Z made it difficult to differentiate between types of hydrometeors and to distinguish between meteorological and non-

Table 1.1: Threshold values for some radar variables for classifying hail. Adapted from Table 2. in Straka et al. 2000.

Hail	Z_h (dBZ)	Z_{dr} (dB)	$\lvert\rho_{hv}(0)\rvert$ (%)	K_{dp} (° km^{-1})
Hail ($D > 5$ mm)	45–80	−2 to 0.5	<0.97	−0.5 to 1
Dry hail ($D > 5$ mm)	45–60	−1 to 0.5	>0.95	0 to 0.5
Wet hail ($D > 5$ mm)	50–80	−2 to 0.5	<0.95	−0.5 to 1
Small wet hail ($D < 20$ mm)	50–60	−0.5 to 0.5	0.92–0.95	−0.5 to 0.5
Large wet hail ($D > 20$ mm)	55–65	−1 to 0.5	0.90–0.92	−0.5 to 1
Giant wet hail ($D > 40$ mm)	60–80	−2 to 0	<0.90	−0.5 to 1

meteorological echoes. The integration of dual polarization has provided much more insight into the physical properties of hydrometeors. For detecting hail, the most commonly used radar variables used are equivalent reflectivity factor (Z_H), co-polar cross-correlation coefficient (ρ_{HV}), differential reflectivity factor (Z_{DR}), and specific differential phase (K_{DP}). The values of these variables vary, depending on the scattering properties of the hailstones and radar wavelength. Table 1.1 illustrates the typical ranges of values for each variable for classifying hail.

2.2.1 Radar Variables

Equivalent reflectivity factor measures the return power that a radar receives after the radar's radiation encounters a scatterer. Reflectivity, one of the moments derived from single-polarization, offers valuable information on the size and concentration of hydrometeors within the radar volume. Radar reflectivity factor is expressed in logarithmic units known as decibels of reflectivity (dBZ). For Rayleigh scattering, reflectivity factor is calculated by:

$$Z_H = \int_0^\infty N(D)D^6 dD \quad (2.1)$$

Reflectivity factor returns for hail are generally higher at S-band than at X-band or C-band due to attenuation issues at the latter two frequencies. It is also important to note that while higher reflectivity values are often associated with larger hailstones, it is also possible for higher reflectivity to indicate a high concentration of smaller hailstones (Kumjian 2013b).

The co-polar cross-correlation coefficient (ρ_{HV}) measures the correlation between the horizontal and vertical backscattered signals within a radar volume, providing an indicator of the similarity among the scatters. Values of ρ_{HV} can range from 0 to 1, where higher ρ_{HV} means greater homogeneity. ρ_{HV} is a unitless variable. A decrease in ρ_{HV} can result from mixed-phase particles, such as melting hail, or scatterers that are very large, have irregular shapes, and have varied orientations (e.g., Picca and Ryzhkov 2012; Kumjian 2013a,b). ρ_{HV} can be calculated using the following formula:

$$\rho_{HV} = \frac{(S_{VV} S_{HH}^*)}{\sqrt{| S_{HH}|^2 | S_{VV}|^2}} \quad (2.2)$$

where S_{VV} and S_{HH} denote the complex scattering amplitudes in the vertical and horizontal planes, respectively. For instance, S_{HH} is the horizontally polarized signal that is transmitted and received; this is done to account for orientation. For hail, ρ_{HV} is typically between 0.6 and 1. Low ρ_{HV} value indicates potential hail presence, as opposed to pure rain, which exhibits a value near 1. Variations in ρ_{HV} also indicate different hail growth processes, with dry hail exhibiting higher ρ_{HV} values while wet hail tends to have lower values (Straka et al. 2000).

Differential reflectivity factor (Z_{DR}) represents the logarithmic difference between the horizontal polarization (Z_H) and vertical polarization (Z_V) of the radar reflectivity factor. Z_{DR} can be calculated by:

$$Z_{DR} = 10\log_{10}\left(\frac{Z_h}{Z_v}\right) = Z_H - Z_V \tag{2.3}$$

In the above equation, Z_h and Z_v (i.e lower-case subscripts) are in linear units, and Z_H and Z_V (i.e upper-case subscripts) are in log units. For hail, Z_{DR} provides information on the shape and size of the hydrometeors. Z_{DR} values of 0 dB or slightly negative may occur if the hailstones are tumbling chaotically as they fall, statistically appearing spherical (Kumjian 2013a). Wet hailstones are stabilized by a water torus around the stone, leading to an increase in Z_{DR} (Kumjian 2013a). For Rayleigh scatterers, positive Z_{DR} values occur when horizontally polarized reflectivity is greater than the vertically polarized reflectivity, indicating that the hydrometeors are wider than they are tall. Conversely, negative or near-zero Z_{DR} suggests the hydrometeors are either spherical or vertically oriented. If the size of the hailstones exceeds the Rayleigh regime, negative Z_{DR} values may occur even in hydrometeors in which the horizontal dimension exceeds the vertical dimension. Thus, regions with negative Z_{DR} are sometimes associated with large hailstones, at least at S-band. Z_{DR} is similar to Z_H, in that both experience attenuation issues at lower frequencies.

Specific differential phase (K_{DP}) is the range derivative of the propagation differential phase shift (Φ_{DP}), which is the difference in the phase shift between the horizontally polarized wave and vertically polarized wave caused by propagation through the atmosphere (and, more specifically, hydrometeors). K_{DP} is often called a derived radar variable, since it is not a base product of the polarimetric data. K_{DP} can be calculated by:

$$K_{DP} = \frac{1}{2}\frac{d\Phi_{DP}}{dr} \cong \frac{\Phi_{DP}(r_1) - \Phi_{DP}(r_2)}{2(r_2 - r_1)} \tag{2.4}$$

Since K_{DP} is not power dependent, it is immune to attenuation and partial beam blockage. In

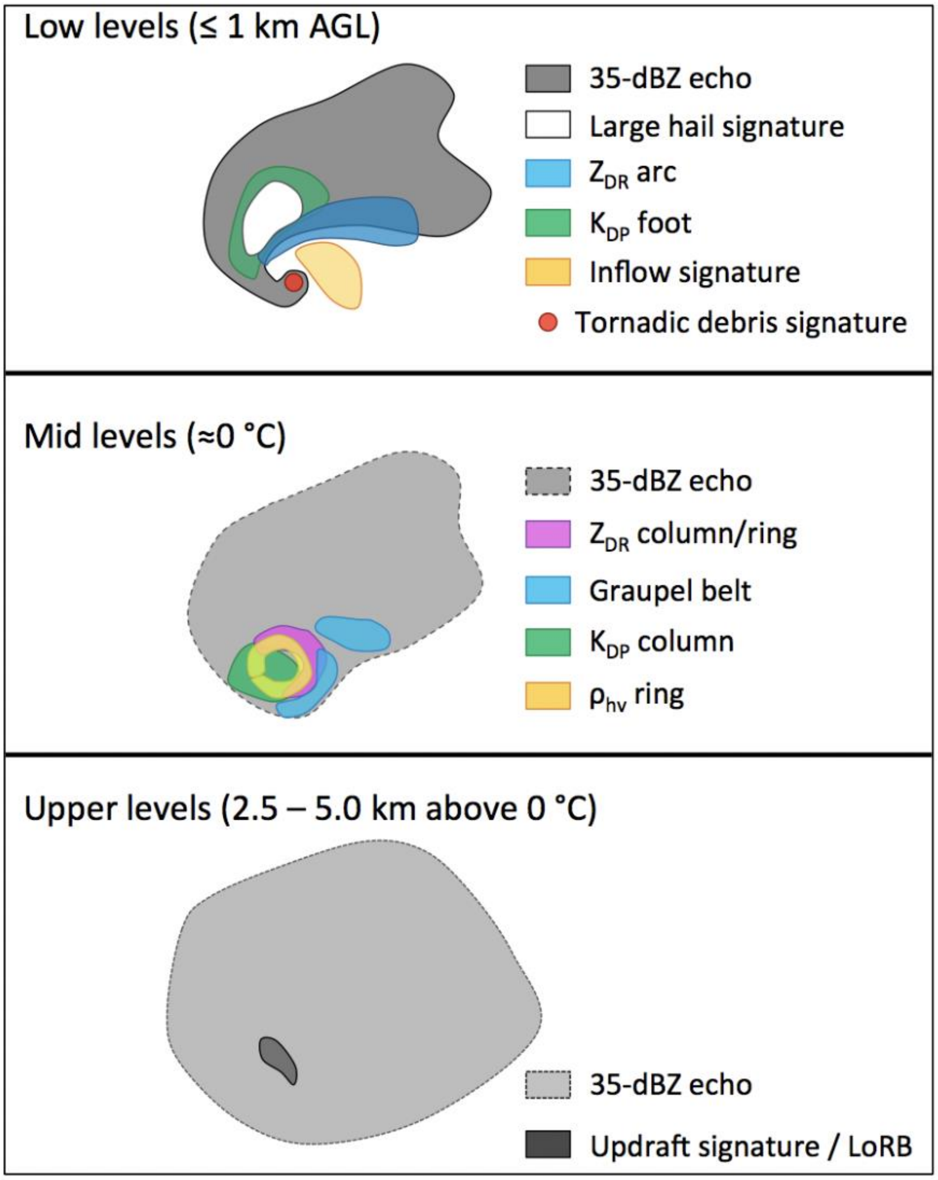

Figure 2.2: Diagram of observed polarimetric signatures at low levels, mid levels, and upper levels. Figure 8 from Kumjian (2013b).

general, hail is associated with values of K_{DP} near-zero. Zero or near-zero K_{DP} values suggest the presence of spherical particles or tumbling hydrometeors, such as hailstones, which have a smaller dielectric constant. Positive K_{DP} values suggest oblate hydrometeors, like raindrops or wet hail, due to water having a higher dielectric constant. Numerous authors (e.g., Hubbert and Bringi (1995); Maesaka et al. 2012; Vulpiani et al. 2012; Schneebeli et al. 2014) have published different techniques for processing Φ_{DP} and estimating K_{DP} each resulting in different K_{DP} fields but retaining the same areas of maximum and minimum K_{DP}. Negative K_{DP} may occur in large hail, especially at C and X-bands. K_{DP} is a good indicator of heavy rain and small melting hail which is a reliable indicator of downdraft regions (Kumijan 2013b).

2.3 Polarimetric Signatures

Polarimetric radar variables reveal specific signatures that indicate current or imminent, future conditions within convective storms. In supercells, notable polarimetric signatures at low levels (< 2 km AGL) include the Z_{DR} arc and K_{DP} foot (Figure 2.2; Kumjian 2013b). The Z_{DR} arc, characterized by high Z_{DR} values greater than 3 dB, forms along the gradient of Z_H in the inflow region of the forward flank downdraft. This feature results from size sorting of hydrometeors where melting hail plays a crucial role in the structure of the Z_{DR} (Dawson et al. 2014). The K_{DP} foot is an area of enhanced specific differential phase observed within the heavy precipitation core of supercells, indicating regions of intense rainfall (Romine et al. 2008). The spatial relationship between the Z_{DR} arc and K_{DP} foot can provide valuable information on tornadogenesis, with a greater separation angle indicating higher tornadic potential (Figure 2.3; Loeffer et al. 2020). Although the exact cause is not fully understood, Loeffer (2020) hypothesizes that a more orthogonal separation of the Z_{DR} and K_{DP} enhancement places the K_{DP} enhancement further into the forward flank of the supercell and away from the updraft. Since K_{DP} is related to precipitation mass content and negative buoyancy production (Carlin and Ryzhkov, 2019), the removal of the K_{DP} enhancement near the updraft may promote tornadogenesis.

At the mid-levels, where the environmental temperature is approximately 0°C, supercells exhibit various polarimetric signatures, including the Z_{DR} column and ring, K_{DP} column, and ρ_{HV}

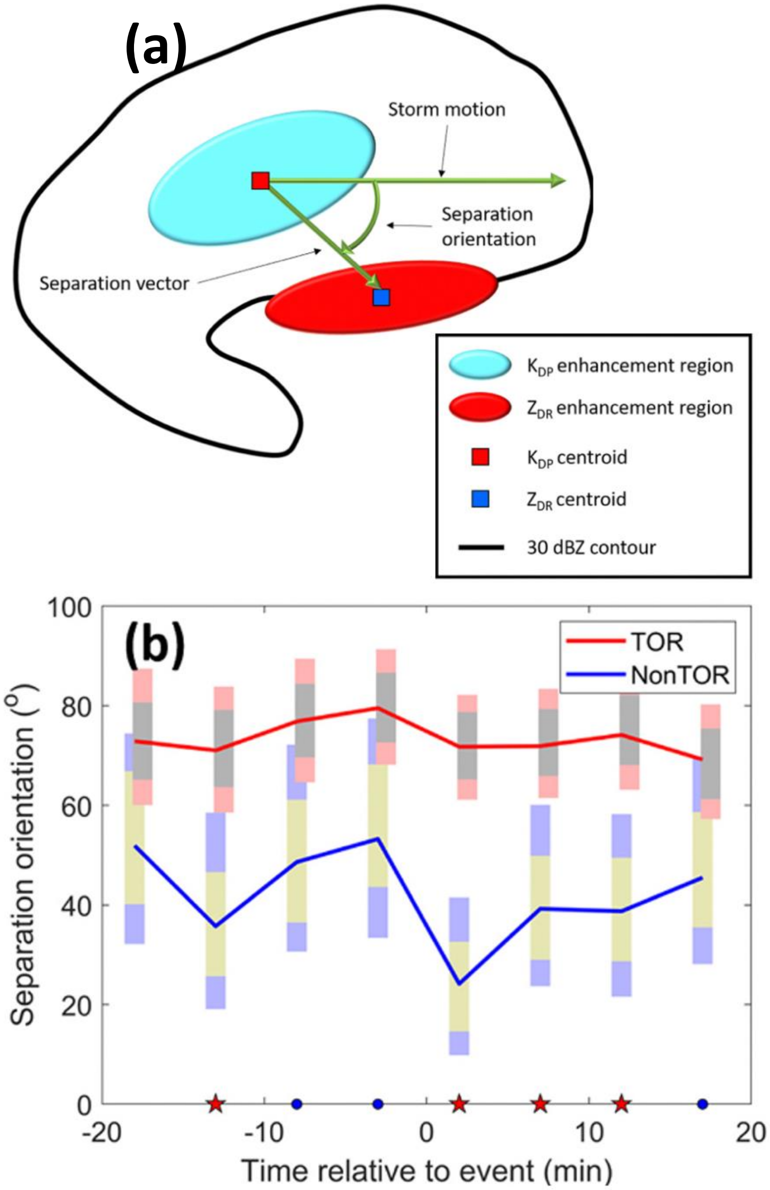

Figure 2.3: (a) Diagram depicting the Z_{DR} and K_{DP} enhancement regions and the separation vector. (b) Graph depicting time series of tornadic vs nontornadic supercells using separation orientation. Figure adapted from Figure 2 and Figure 5b from Loeffer et al. (2020).

ring (Figure 2.2). The Z_{DR} column is a vertical structure of enhanced Z_{DR} values extending upward from the environmental 0°C level and is composed of supercooled liquid drops and wet ice particles situated west of the updraft (Conway and Zrnic 1993). An increase in the height of the

Z_{DR} column, indicating stronger updrafts, often leads to more intense hail at the surface after 10 to 15 minutes (Kumjian 2013b). Similarly, the K_{DP} column is a vertical column of positive K_{DP} values extending from the environmental 0°C level, usually located west or northwest of the Z_{DR} column (Hubbert et al. 1998; Kumjian 2013b). This column consists of a high concentration of small to medium raindrops and melting ice particles. Z_{DR} columns can be distorted into a ring or a half-ring shape by the mesocyclone, called the Z_{DR} ring (Snyder et al. 2013, Kumjian and Ryzhkov 2008). This ring coincides with a similarly shaped area of low ρ_{HV} called the ρ_{HV} ring. These rings encircle the updraft, and when not a complete ring, the Z_{DR} half rings are positioned on the inflow side of the updraft (Kumjian and Ryzhkov 2008). These signatures result from the horizontal advection of wet ice hydrometeors above the freezing level (Kumjian and Ryzhkov 2008). These signatures contain mixed-phase ice, leading to positive Z_{DR} and low ρ_{HV}.

2.3.1 Hail Signature

Hail frequently occurs in severe convective storms, and its identification on radar varies based on radar frequency. Distinct characteristics separate dry hailstones from raindrops via radar. Rain typically shows high Z_H and Z_{DR} values. Small wet hail, which has a stabilizing water torus, appears similar to large raindrops on radar, exhibiting a high Z_{DR}. In. contrast, larger hailstones are usually drier and tumble more, resulting in a chaotic orientation that leads to Z_{DR} values close to zero (Kumjian and Ryzhkov, 2008). At S-band, high Z_H and low Z_{DR} at the lowest elevation strongly indicate large hail reaching the ground (Figure 2.4). However, this is not universal across all frequencies; an example is at X-band, large hail may have observed Z_H values below 50 dBZ (Snyder et al. 2010). Another useful polarimetric variable for identifying hail is ρ_{HV}. A decrease in ρ_{HV} indicates less homogeneity among the hydrometeors. Small wet hail can produce ρ_{HV} values

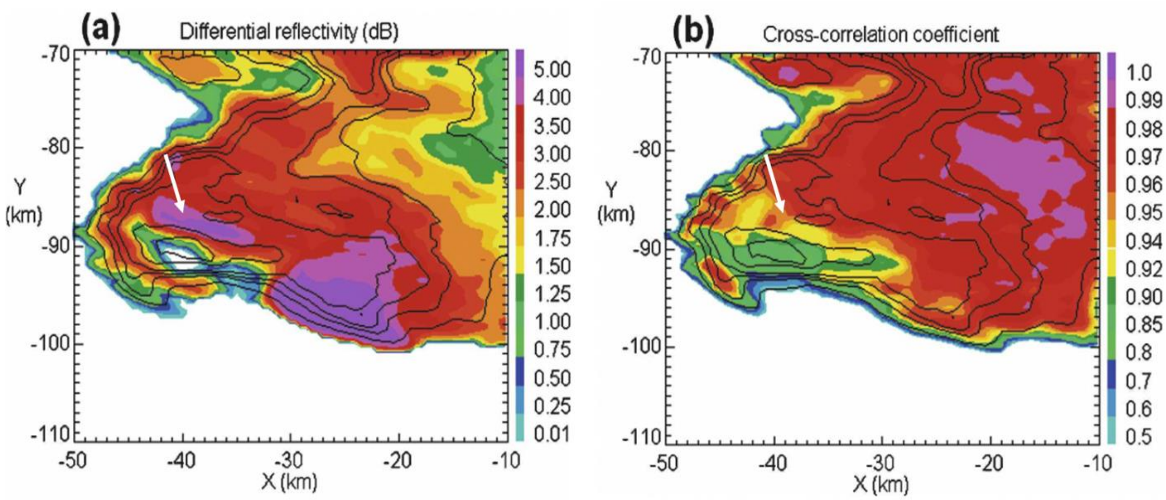

Figure 2.4: Example of a hail signature at S-band denoted by the white arrow. Adapted from Figure 3 in Kumjian and Ryzhkov (2008).

less than 0.95, while very large hail can lead to ρ_{HV} values below 0.85.

2.3.2 Low Reflectivity Ribbon (LRR)

The low reflectivity ribbon (LRR) is a distinct band of reduced Z_H and Z_{DR} that extends from the hook echo into the forward flank of a supercell (Snyder et al. 2013). Typically observed within the lower 3 km of the storm, the LRR shows a reduction in Z_H by 5 to 15 dB*Z* with local reductions exceeding 20 dB*Z* (Wurman et al. 2012; Snyder et al. 2013). At X-band, Z_{DR} values within the LRR are generally 0 to 2 dB. The LRR can also appear in other polarimetric variables, such as ρ_{HV} and Φ_{DP}, though these values can vary significantly between cases (Snyder et al. 2013). K_{DP}-based attenuation correction often introduces streakiness in the Z_H and Z_{DR} fields due to the accumulation of noise and small errors in K_{DP} over long distances, which increase during the integration process used for the attenuation correction. Therefore, figures depicting the LRR will show the observed (uncorrected) Z_H and Z_{DR} fields. Analysis done by Griffin et al. (2018) indicates that the LRR is associated with cyclonic vertical vorticity aloft, and they also hypothesize that the LRR is composed of sparse, large hail. Figure 2.5 illustrates the observed Z_H, Z_{DR}, ρ_{HV},

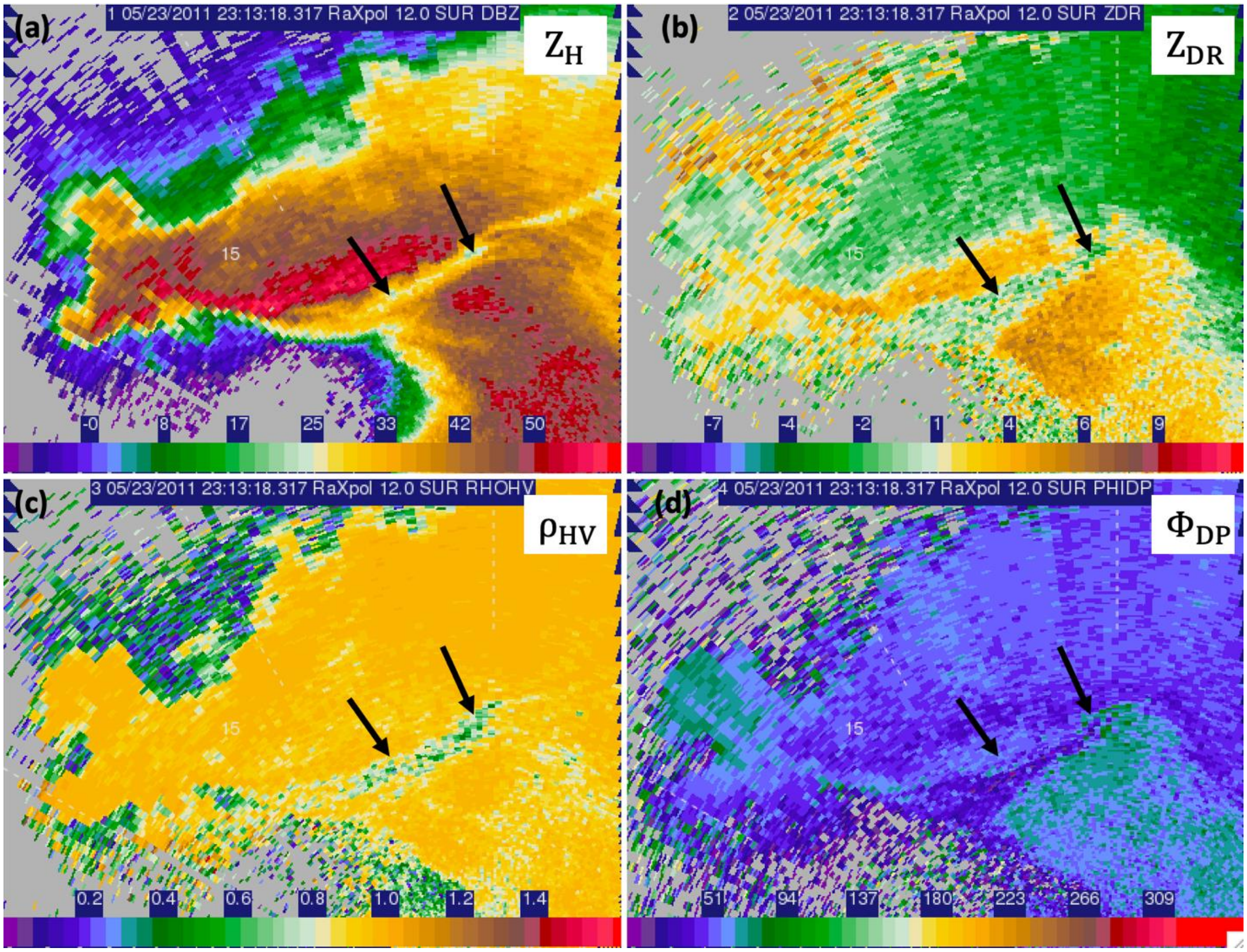

Figure 2.5: PPIs from RaXPol of (a) Z_H, (b) Z_{DR}, (c) ρ_{HV}, and (d) Φ_{DP} observations that illustrate an LLR in the 23 May 2011 hailstorm. Arrows mark the position of the LRR in each panel.

and Φ_{DP} fields from RaXPol of the 23 May 2011 hailstorm at 2313 UTC at 12.0° in elevation (2.8 km above radar level). This figure shows a ribbon of low Z_H, Z_{DR}, and ρ_{HV} extending from the hook of the supercell to the end of the forward flank. In the LRR, Z_H values are 20 to 25 dB*Z* lower than the surrounding areas, and Z_{DR} values are 3 to 5 dB lower, which aligns with the stated literature values. Values of ρ_{HV} are approximately 0.4 lower than the adjacent areas. The LRR was visible throughout the entire volume scan, lowest elevation to the highest level.

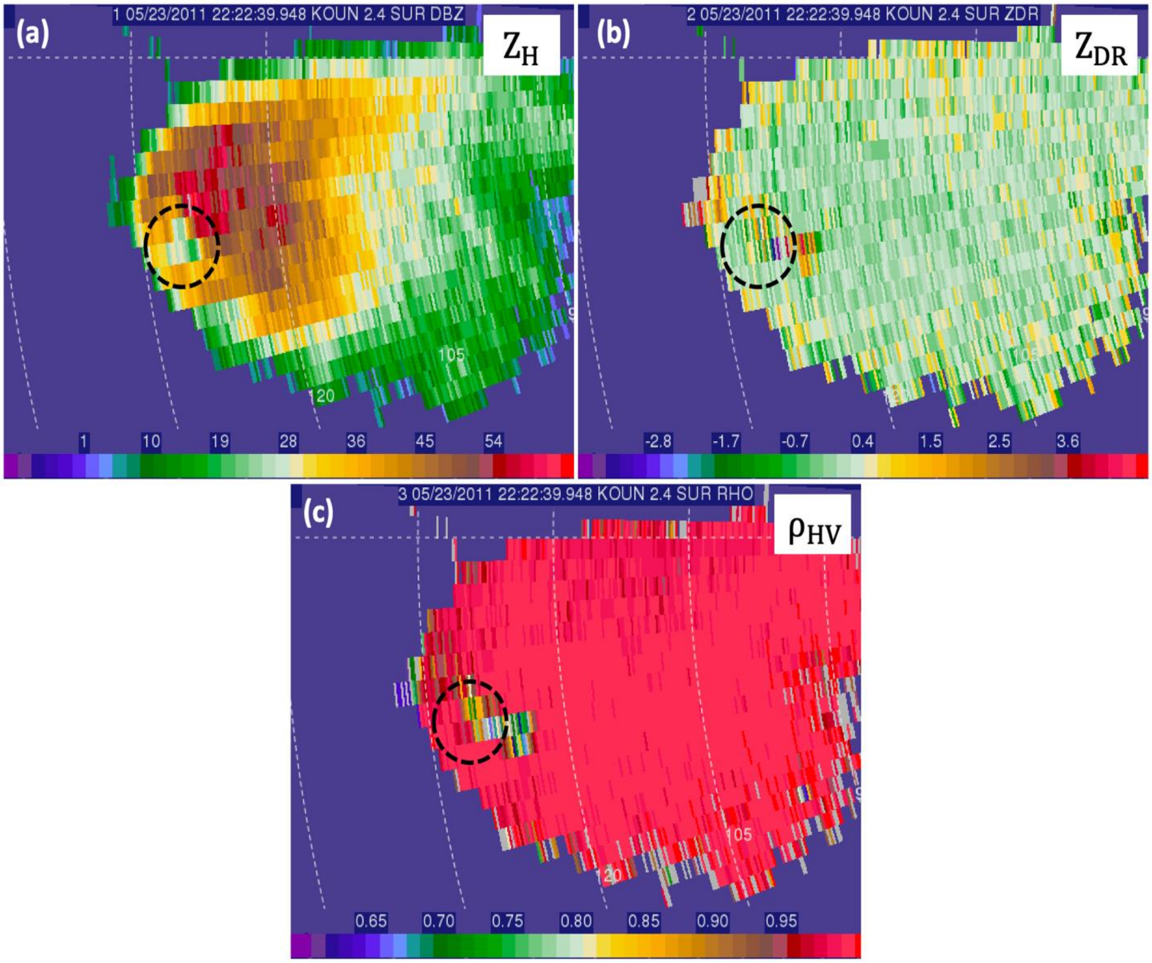

Figure 2.6: PPIs from KOUN of (a) Z_H, (b) Z_{DR}, and (c) ρ_{HV} observations that illustrate a BWER in the 23 May 2011 hailstorm. Dashed circles mark the location of the BWER in each panel.

2.3.3 Bounded Weak Echo Region (BWER)

A bounded weak echo region (BWER) is a region of low Z_H values surrounded by higher Z_H values (Chisolm 1973). This signature is associated with a strong updraft near and occurs due to dearth of hydrometeors in the presence of very rapid upward advection of precipitation in intense updrafts. The BWER is typically found to be offset from the Z_{DR} column (Snyder et al. 2013). Figure 2.6 displays a BWER observed during the 23 May 2011 hailstorm. This signature was observed by KOUN at approximately 2223 UTC at 2.4° in elevation. Figure 2.5 also shows polarimetric variables Z_{DR} and ρ_{HV} in panels b and c, respectively. High values of Z_{DR} and low values of ρ_{HV} are seen slightly offset to the right of the BWER.

2.3.4 Weak Echo Hole (WEH)

A weak echo hole (WEH) refers to an area, typically within the hook echo of a supercell characterized by a local minimum in Z_H. It can be described as a micro-scale version of the eye of a hurricane. The formation of the WEH is typically due to the centrifuging of hydrometeors or debris away from the center of a tornado. The term "WEH" was first introduced by Fujita (1958). Recent high-resolution data from mobile Doppler radars have shown that the vortex center often alights closely with the WEH (Weinhoff et al. 2020). However, the WEH often closes near the surface due to the effects of frictional convergence or debris that has yet to be centrifuged (Bluestein et al. 2004; Houser et al. 2016). It is important to note that the presence of a WEH does not necessarily indicate the presence of a tornado but could indicate a weaker vortex.

2.3.5 Tornado Debris Signature (TDS)

The tornado debris signature (TDS) is a region of significantly reduced ρ_{HV} and often near-zero values of Z_{DR} co-located with a strong velocity couplet (Ryzhkov et al. 2005). TDSs form when a tornado lofts debris of various sizes, shapes, and orientations. Typically, ρ_{HV} values in a TDS are less than 0.8. Although Z_{DR} can approach zero in tornadic debris, this signature is less reliable compared to reduced ρ_{HV}. If raindrops mix with the lofted debris, Z_{DR} values may increase, reducing the low-value Z_{DR} signature in the TDS (Bluestein et al. 2007). The TDS may not appear for various reasons. It might not appear in weaker tornadoes or if the tornado is occurring in rural areas or in open fields due to the lack of lofted debris. At farther distances, beam broadening may occur, where the radar resolution volume becomes too large, and it may not resolve the signature. Ryzhkov et al. (2002) first noted the reduction in polarimetric signatures associated with tornadic debris in the hook echo of a supercell using an S-band radar. Ryzhkov et al. (2005) found that the TDS is a reliable indicator of strong tornadoes (EF3 or greater on the enhanced Fujita scale). Kumjian and Ryzhkov (2008) note multiple instances of weaker tornadoes also producing TDSs at S-band. This has also been confirmed in studies using C-band (Ryzhkov et al. 2007a) and X-band (Bluestein et al. 2007) radars. The TDS is a reliable radar-based indicator of an ongoing tornado.

2.3.2 Three-body Scatter Spike (TBSS)

Large hail in a supercell can result in a Three-Body Scatter Spike (TBSS), or hail spike, a radar artifact indicating large hail at that elevation angle. It appears as a spike of low reflectivity radially downrange from a high reflectivity core and is detectable at various elevation angles. This artifact occurs when radar signals are side-scattered by large hydrometeors toward the ground, then back to the radar, resulting in a delayed return signal. Although the TBSS does not directly indicate hail size, it is often associated with large hail cores (Lemon 1998; Zrnic et al. 2010). Lemon (1998) suggests a hail diameter above 2.5 cm is necessary for the artifact. The TBSS is known to precede surface hailfall and strong winds by 10 to 30 minutes (Lemon 1998; Battaglia et al. 2010). Figure 2.7 shows a prominent TBSS at 2312 UTC observed by RaXPol. The TBSS can be seen in Z_H, spectrum width (W) and in polarimetric variables such as Z_{DR}, and ρ_{HV}. The TBSS appears throughout the scanning period of RaXPol, varying in size across different elevation angles.

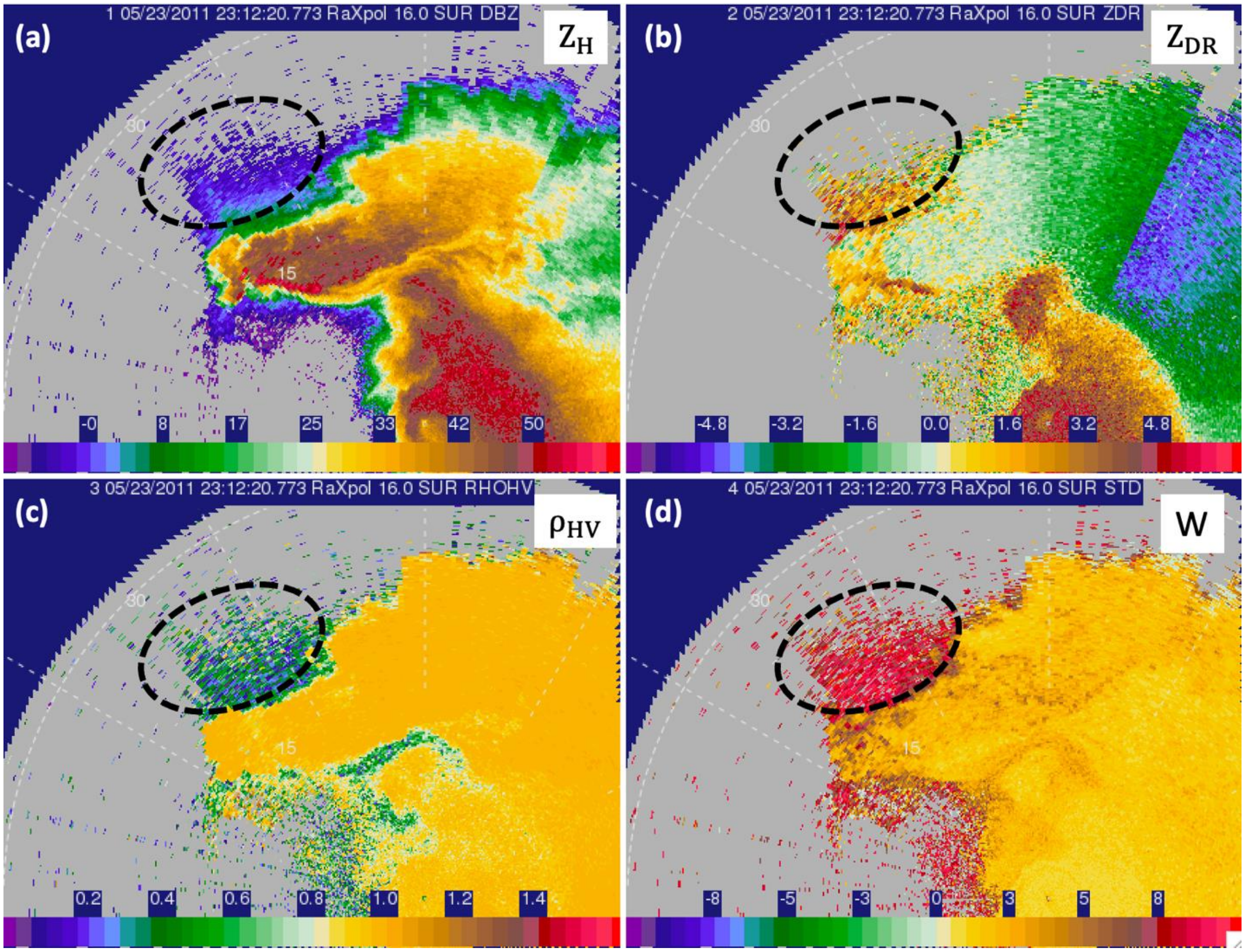

Figure 2.7: PPIs from RaXPol of (a) Z_H, (b) Z_{DR}, (c) ρ_{HV}, and (d) W observations that illustrate a TBSS in the 23 May 2011 hailstorm. Dashed circles mark the position of the TBSS in each panel.

Chapter 3

Data and Methods

3.1 Instrumentation Overview

3.1.1 The Mobile, Rapid-Scan, X-band, Polarimetric, Doppler Radar (RaXPol)

RaXPol is a mobile, X-band, polarimetric Doppler radar maintained by the Advanced Radar Research Center at the University of Oklahoma. It features a 2.4 m mechanically rotating parabolic dish mounted on a heavy-duty truck (Figure 3.1; Pazmany et al. 2013). RaXPol operates at a frequency of 9730 MHz and a wavelength of 3.08 cm. Since becoming operational in 2011, RaXPol quickly became an innovative tool for collecting data on rapidly evolving storms due to its rapid scan and dual-polarization capabilities.

One of RaXPol's notable features is its rapid scanning capability, which allows the antenna to scan at an azimuthal scanning rate as fast as 180° s^{-1}. To ensure the collection of a sufficient number of independent samples, RaXPol employs a frequency hopping strategy. This strategy involves transmitting 24 pulses in 12 pairs, with each pair's pulse frequency shifted by an amount equivalent to the pulse's beamwidth. This frequency hopping technique not only facilitates the collection of independent samples but also suppresses second trip echoes in the first sample of the pulse pair. From these samples, signal power from the horizontal and vertical channels, as well as, the co-polar cross-correlation coefficient, are estimated (Pazmany et al. 2013).

Figure 3.1: Image of RaXPol photographed by the author near Canadian, TX, on 01 May 2024

As a mobile radar, RaXPol can be rapidly deployed in approximately two minutes and in close proximity to tornadic supercells and other sub-storm-scale phenomena, enabling data collection in the lower levels of storms. Utilizing the radar's rapid scanning mode, a volume scan consisting of 10 elevation angles can be done in approximately 20 seconds. The combination of mobility, dual-polarimetric capabilities, and a quick volumetric update time makes RaXPol a unique tool for data collection in storms.

However, RaXPol does have some drawbacks. Since RaXPol is an X-band radar, it is highly affected by attenuation in heavy precipitation. To counter this issue, attenuation correction techniques utilizing dual-polarimetric data, like those outlined in Snyder et al. (2010), need to be applied to the data.

Figure 3.2: Image of NOXP in Colorado during a field campaign focused on observing rain and snowfall to improve forecasts in mountainous regions. Photograph taken from NSSL's mobile radar webpage.

3.1.2 The National Severe Storms Laboratory Dual-Polarized, X-band Radar (NOXP)

NOXP is a mobile, dual-polarimetric, X-band radar used by NOAA's National Severe Storms Laboratory (Figure 3.2). Operational since 2009, NOXP has participated in numerous research experiments, focusing on severe weather, winter storms, and even bat migration patterns. NOXP can quickly be set up to collect data in various conditions with an approximate deployment time of 5 minutes. It can conduct a volume scan of 15 elevation angles in approximately 3 minutes.

Operating at a frequency of 9410 MHz and a wavelength of 3.21 cm, NOXP has an effective range of 130 km and a 0.9° 3-db beamwidth. These specifications make NOXP a valuable tool for collecting data on meteorological phenomena. However, like other X-band radars, NOXP is subject to attenuation in heavy precipitation, which can affect the collected data quality. Another limitation of this radar is the lack of rapid scanning technology. While dual polarization provides

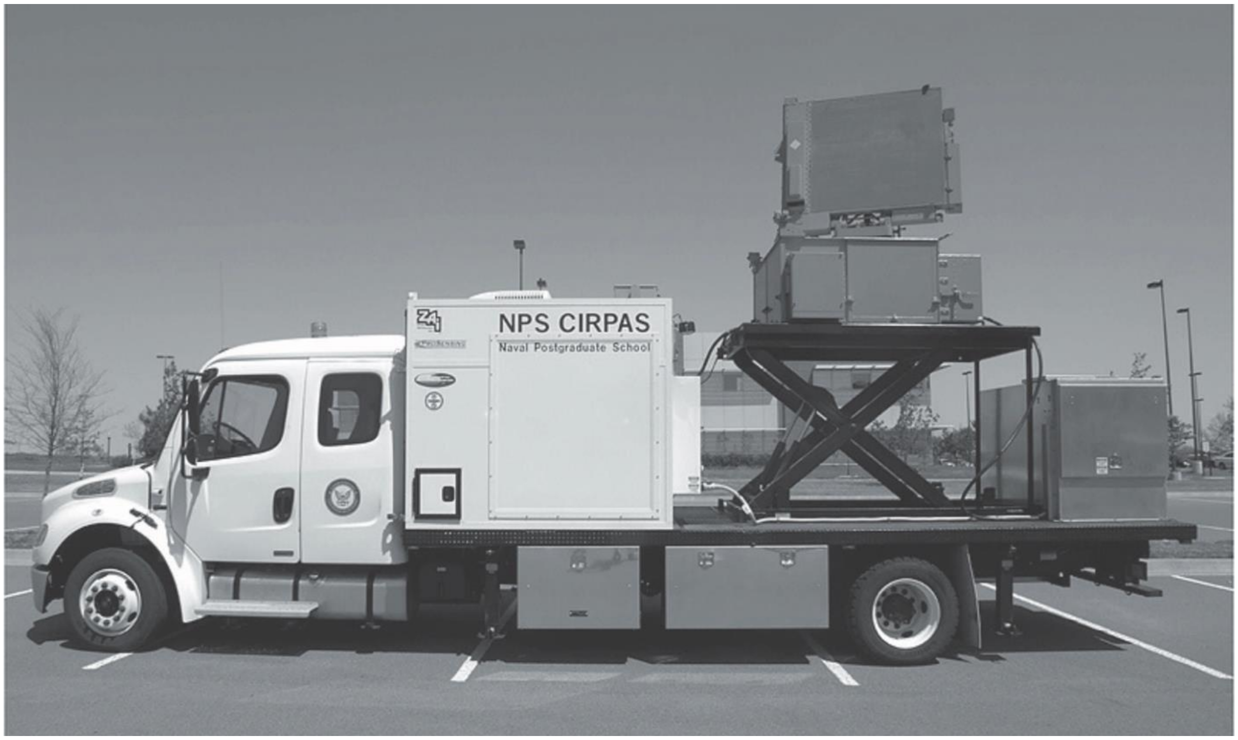

Figure 3.3: Image of MWR-05XP photographed by H. Bluestein. Adapted from Bluestein et al. 2010.

information on the size, shape, and orientation of hydrometers, observing their evolution may be difficult without rapid scanning technology.

3.1.3 The Meteorological Weather Radar 2005 Phased Array (MWR-05XP)

The Meteorological Weather Radar 2005 Phased Array (MWR-05XP) is a modified air defense tactical radar that is mounted on the bed of a heavy-duty truck (Figure 3.3; Sandifer 2005). It features a hybrid antenna that scans electronically in elevation and mechanically in azimuth. Although the MWR-05XP can perform electronic azimuthal scanning, this capability is primarily used to minimize beam smearing. The radar can be deployed in approximately five minutes, making it a viable tool for collecting rapid-scan data in supercells and tornadoes (Bluestein et al. 2010).

Table 3.1. Comparison of radar characteristics

	RaXPol	NOXP	MWR-05XP	KFDR	KOUN
Frequency	9.71– 9.75 GHz	9.42 GHz	9.3 – 10 GHz	2.91 GHz	2.75 GHz
Transmit Power	20 kW	250 kW	≥ 15 kW	475 kW	450 kW
3 db Beamwidth	1° (1.4°)[1]	1°	1.8°	0.91°	1.0°
Range Resolution	75 m	74 m	150 m	250 m	250 m
Rotation Rate	180°	29°	180°	30°	30°
Dual-Polarization	Yes	Yes	No	No[2]	Yes

Like RaXPol, MWR-05XP employs a frequency hopping technique when scanning electronically in azimuth. Frequency hopping occurs at every other pulse, allowing the beam's phase to change as the frequency changes. Electronic elevation scanning is achieved using phase shifters, which adjust the phase delay among the antenna elements. The radar has an azimuthal scanning rate of 180° s^{-1} and frequency hopping facilitates the collection of more independent samples.

MWR-05XP utilizes two different scanning strategies: a stepped frequency spiral (STF-SP) and a stepped frequency elevation (STF-E) (Bluestein et al. 2010). The STF-SP is a volumetric scanning strategy that covers a full 360° in azimuth by overlapping elevation angles. This mode is similar to the one used by operational NEXRAD radars but is approximately 10 times faster, completing a full-volume scan in approximately 25 seconds. This scanning strategy is ideal for covering large areas with multiple convective storms. The second strategy, STF-E, conducts a volumetric sector scan. In this mode, the antenna's elevation angle changes electronically after rapidly transmitting a pair of radar pulses through the set elevation angle. Ten

[1] 1.4° due to beam smearing (Pazmany et al. 2013)
[2] KFDR obtained polarimetric capabilities in 2012

sequential pulses are transmitted at the same elevation level and then averaged to obtain estimates of reflectivity and velocity. This was repeated for every elevation angle. A 90° sector scan can be completed in approximately 13 seconds.

With its rapid scanning ability and high temporal resolution, MWR-05XP is a useful radar for collecting data on storms in close range. However, one limitation of this radar is the lack of dual-polarization capabilities, making it difficult to gather information on the types of scatters. Additionally, MWR-05XP has a beamwidth of 1.8°, which is almost twice as large as other X-band mobile radars. Therefore, Bluestein et al. (2010) advises that MWR-05XP is better suited for storm-scale processes rather than sub-storm-scale processes.

3.1.4 A NEXRAD WSR-88D Radar (KFDR)

KFDR is the operational WSR-88D located in Frederick, Oklahoma. The operational radar network utilizes S-band radars. Before 2012, this NEXRAD site did not have polarimetric capabilities. Being an S-band radar, KFDR operates at a longer wavelength, which means it is less affected by attenuation compared to X-band mobile radars. The longer wavelength and higher power output enables KFDR to observe more storms at a greater distance than the mobile radars. This capability allows KFDR to capture the full evolution of storms and provides more insight into the vertical depth of storms. However, as a fixed-position radar, KFDR cannot get into close proximity to most of the storms. Additionally, KFDR has a slower scanning rate than that of RaXPol, taking approximately 5 minutes to conduct a full volumetric scan.

Figure 3.4: Photograph of KOUN collecting data on a thunderstorm in Norman, Ok. Photo by. Charles Kuster, OU CIMMS/NSSL

3.1.5 The National Severe Storms Laboratory's WSR-88D Radar (KOUN)

KOUN is the National Severe Storm Laboratory's research WSR-88D radar located at Max Westheimer Airport in Norman, Oklahoma (Figure 3.4). Like other radars in the NEXRAD network, KOUN is an S-band radar often used for severe weather observations. It has polarimetric capabilities, allowing it to resolve information on the characteristics of hydrometeors. Similar to KFDR, KOUN operates at a longer wavelength, which means it is less affected by attenuation. KOUN can be operated in a sector scan mode, providing volumetric update times of approximately 90 seconds, which is faster than the operational radar network. A comparison of all five radars is shown in Table 3.1.

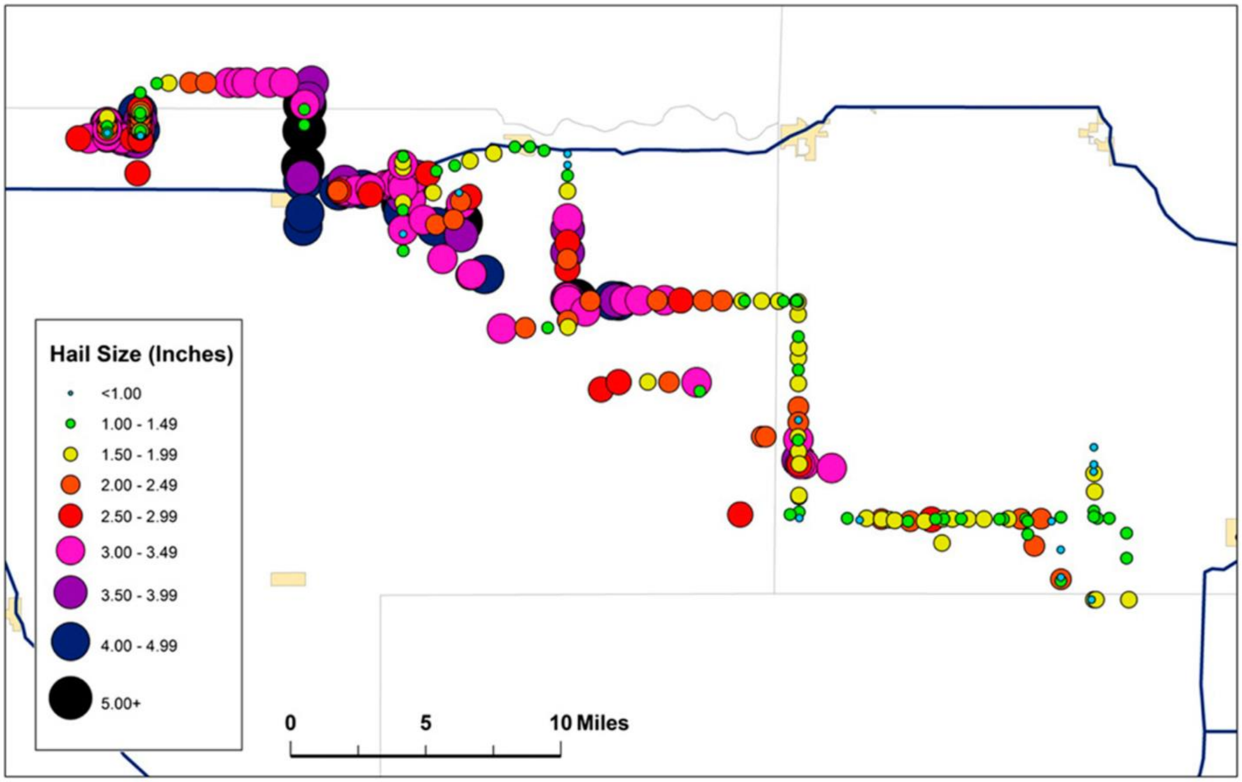

Figure 3.5: Hail reports collected by HailSTONE on 23 May 2011 from a supercell in southwestern OK. Figure adapted from Figure 2 in Blair et al. (2017).

3.2 HailSTONE Field Campaign

During the HailSTONE field campaign, data were collected from 73 severe thunderstorms that produced hail ≥ 1.00 in (Blair et al. 2017). This campaign aimed to gather high-resolution ground measurements to enhance hail size forecasting by the National Weather Service (NWS) and improve giant-hail climatology. This extensive data collection from these 73 severe thunderstorms offers valuable insights into storm characteristics. On 23 May 2011 alone, 230 hailstones were collected (Figure 3.6), varying in size from 0.25 in (0.64 cm) to 6.00 in (15.24 cm) (Figure 3.5). The data from the HailSTONE field campaign will be integrated with the radar data to show the spatial distribution of the hailstones relative to the supercell.

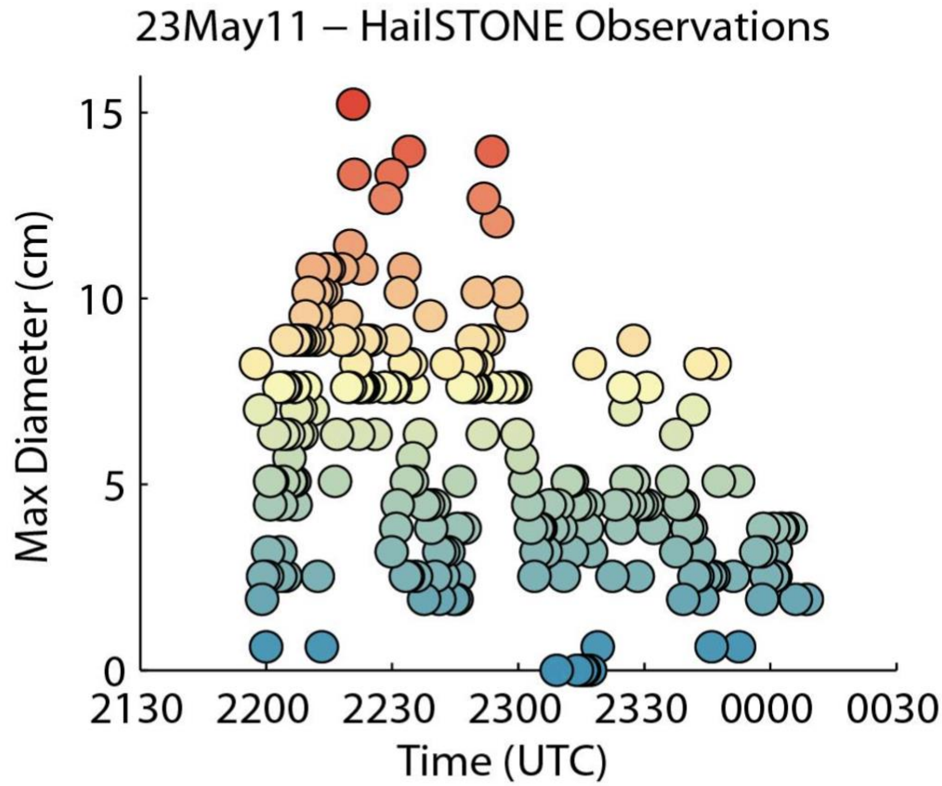

Figure 3.6: HailSTONE observations of the collected hailstones plotted as a function of space and time. Adapted from Snyder et. al 2014

3.3 Data Quality Control

Various factors influence the quality of data collected by weather radars, including the radar type and environmental conditions in the sampled area. For example, the rapid scanning rate of RaXPol and MWR-05XP can result in beam smearing (Pazmany et al. 2013). Deployment locations can also affect data quality; for mobile radars, being near trees or hills can degrade data. Additionally, selecting an appropriate pulse repetition frequency (PRF) is critical to ensure good data quality. The Doppler dilemma arises when choosing a large PRF to achieve a large unambiguous velocity, compromising the unambiguous range and vice versa (Doviak and Zrnic 1993). On the day of the 23 May 2011hailstorm, RaXPol transmitted with a high PRF, resulting in a large unambiguous velocity but second trip echoes occurred. Moreover, the presence of hail in a supercell can produce a three-body scatter spike (TBSS), commonly referred to as a hail spike (discussed in section 2.3.3). To address these challenges, data from all five radars were inspected and, when necessary, corrected using a quality-control process.

The data from all five radars were manually edited using Solo3, a software package developed by the National Center for Atmospheric Research (NCAR) (Oye et al. 1995). Initially, the data underwent a despeckling process. The "despeckle" command in Solo3 removes individual pixels and groups of fewer than four pixels from the radar field, which can be considered noise. Next, upper and lower thresholds were applied to RaXPol and NOXP to remove a hail spike and second trip echo. To address the second-trip echoes, a threshold value was set to exclude all values where the standard deviation or spectrum width exceeded 12 ms^{-1} to address second-trip echoes. The criteria for identifying and removing hail spikes included low reflectivity, low ρ_{HV}, and high spectrum width. Specifically, areas with ρ_{HV} below 0.5 and spectrum width above 6.0 ms^{-1} were filtered out. This condition was applied to both RaXPol and NOXP. A threshold removing reflectivity values greater than 100 dBZ was also applied to RaXPol due to a pixel having a value of 300 dBZ near the RaXPol radar. After removing unwanted artifacts, radial velocities were manually unfolded in and around the mesocyclone as well as in the outer areas of the storm for the X-band radars. Due to differing PRFs, the Nyquist velocities for each radar varied. RaXPol had a Nyquist velocity of 30.83 ms^{-1}. NOXP and MWR-05XP had similar Nyquist velocities of 19.94 ms^{-1}, and 19.54 ms^{-1} respectively. For the S-band radars, the data were despeckled, ensuring the dryline remained visible to indicate where the storm formed relative to the dryline. For the S-band radars, the velocities did not need to be dealiased.

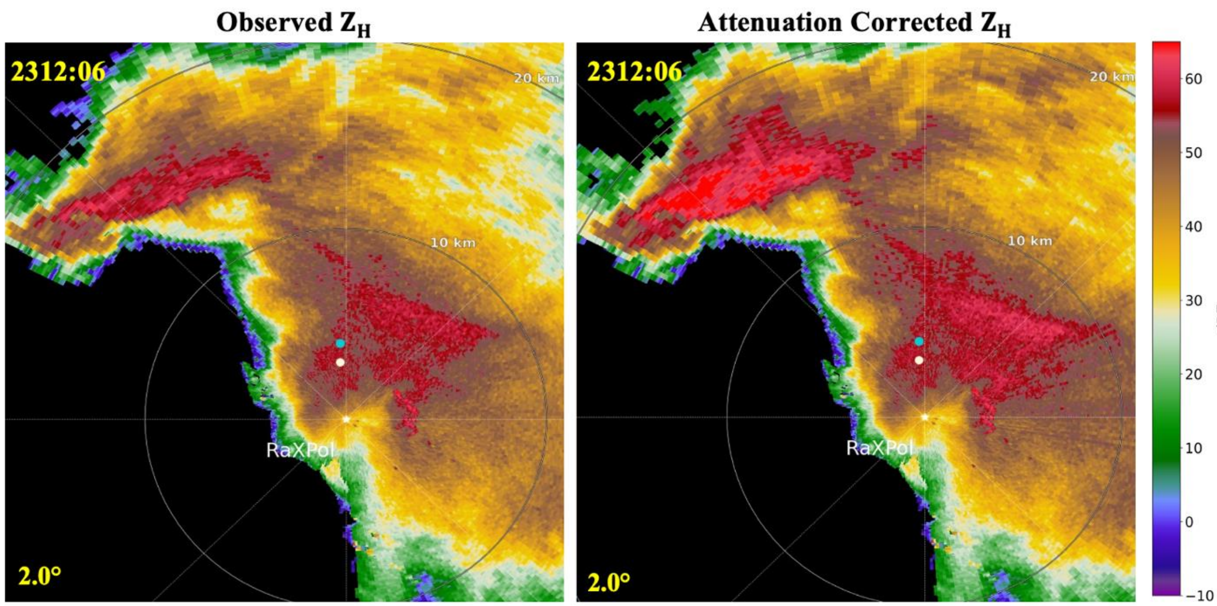

Figure 3.7: Comparison of the observed and the attenuation-corrected reflectivity fields. The largest attenuation occurred in the hook echo of the supercell.

3.3.1 Specific Differential Phase Calculation and Attenuation Correction

As stated earlier, X-band radars are subject to strong attenuation in heavy precipitation. Since two of the radars were X-band polarimetric radars, attenuation correction needed to be applied to the data. For a correction technique to be applied, K_{DP} needed to be calculated. While NOXP computed a K_{DP} field, it appeared to be ~2x that of RaXPol; further investigation revealed that NOXP may not have provided the two-way range derivative of differential phase, rather than the more commonly used definition of K_{DP} that is one-half the range derivative, causing the K_{DP} values to be double what they should be. To correct this issue, the K_{DP} field for NOXP was divided by 2. For RaXPol, K_{DP} needed to be calculated. The updated version of the Hubbert and Bringi method (Hubbert and Bringi, 1995; Stepanian et al. 2016) from the Lidar Radar Open Software Environment (LROSE) was used to compute K_{DP} and perform attenuation correction. LROSE is an open-source software developed by Colorado State University and NCAR (DeHart et al. 2023).

The calculation of K_{DP} begins with the unfolded differential phase (ϕ_{DP}). A finite impulse response (FIR) filter was applied twice to create a smoothed ϕ_{DP} field. Peaks in the smoothed ϕ_{DP} field were then removed to create a conditioned ϕ_{DP} field, eliminating local increases due to the backscatter differential phase. Another application of the FIR filter was done twice on the conditioned ϕ_{DP} field to improve smoothing. K_{DP} is than calculated by the slope of the conditioned ϕ_{DP} in range divided by 2 (Hubbert and Bringi, 1995; Stepanian et al. 2016). The ZPHI method described by Bringi and Chandrasekar (2001) and Snyder et al. (2010) was used for attenuation correction.

Attenuation is proportional to liquid water content and shows a near-linear relationship with K_{DP} for radar frequencies between 5-19 GHz (Bringi and Chandrasekar 2001). The relationship between attenuation and K_{DP} can be expressed as a power law:

$$A_H = \alpha K_{DP}^b \tag{3.1}$$

$$A_{DP} = \beta K_{DP}^b \tag{3.2}$$

where A_H represents the attenuation of Z_H and A_{DP} represents the (differential) attenuation of Z_{DR}. The default LROSE coefficients are those specified in Table 7.1 in Bringi and Chandrasekar (2001). Since NOXP and RaXPol have frequencies of 9.4 GHz and 9.7 GHz respectively, the default coefficients in LROSE were adjusted to those specified in Snyder et al. (2010). The coefficients were changed to α = 0.313 and β= 0.0483. A comparison between the observed reflectivity and attenuation corrected reflectivity field is shown in Figure 3.7. The attenuation correction was verified by qualitatively comparing it with the S-band Z_H and of Z_{DR}fields.

3.4 Radar Analysis

The radar data were visualized using a plan position indicator (PPI) display. The data were cleaned and then thoroughly analyzed to identify storm-scale features such as rear flank gust fronts (RFGFs), cyclonic vortex signatures, or weak echo holes (WEHs). To identify these features, animations of Z_H, V_r, and polarimetric variables (when applicable) were viewed in Solo3. Given the simultaneous scanning of multiple radars, a multi-Doppler analysis was done to get insight into the 3-D wind field. The multi-Doppler analysis was carried out using LROSE's SAMURAI, a variational analysis technique described in Bell et al. (2012). The parameter files were edited to account for each radar, and a background file, which was a sounding launched at 18z. The sounding provides the technique with an a priori estimate of the wind field. The output files were visualized using Py-ART (Helmus and Collis 2016). Alongside the 3-D wind field, information on the types of hydrometeors in the storm was also sought. A hydrometeor classification algorithm (HCA) was run on the data to determine the dominant hydrometeor type within areas of the storm. This was done using LROSE's RadxPid, which uses polarimetric data to estimate the dominant hydrometeor type using NCAR's Particle Identification algorithm. RadxPid uses a fuzzy logic algorithm to calculate the HCA outlined in Vivekanandan et al. (1999). The output from these analyses will be presented in Chapter 5.

Chapter 4

The 23 May 2011 Hailstorm

4.1 Synoptic Overview

On 23 May 2011, around 1500 UTC, a low-pressure area of approximately 1002 hPa was located in the far northeastern Texas panhandle. This low-pressure system had a dryline extending southwestward into west Texas (Figure 4.1). East of the dryline, surface dewpoints were relatively high, ranging from the upper 60s to the lower 70s ºF. The low-level convergence was expected to increase along and east of the dryline. This, combined with the large-scale ascent from a shortwave trough moving into the Southern Plains from the west, was the trigger for convective initiation.

The 1200 UTC sounding from OUN in Norman, OK (Figure 4.2), sampled a potentially unstable environment characterized by the mixed-layer convective available potential energy (MLCAPE) of 4900 J kg^{-1}, and a surface dewpoint of 72ºF (22°C). Convective initiation in Oklahoma began at approximately 2000 UTC, with storms appearing east of the dryline in areas where surface-based CAPE (SBCAPE) ranged from 4000 to 5000 J kg^{-1} (Figure 4.3c). Figure 4.3 provides an overview of the synoptic environment, highlighting areas of moisture (Figure 4.3b), strong instability (Figure 4.3c), and a deep shear layer of approximately 40 to 45 knots (20 to 23 ms^{-1}) (Figure 4.3d). Additionally, the low-level jet had values of 20 knots (10 ms^{-1}) at 850 mb (Figure 4.3b) which further contributed to this environment. These conditions created a favorable

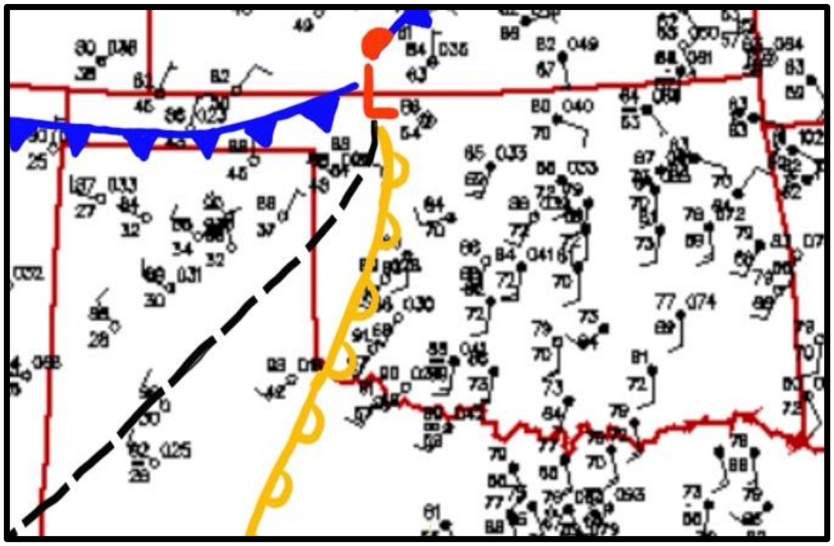

Figure 4.1: Surface analysis on 23 May 2011, valid at 1800 UTC. Adapted from the Plymouth State Weather Center Surface Map Archive. Location of a cold front and dry line, associated with the low-pressure area, is shown in blue and yellow, respectively.

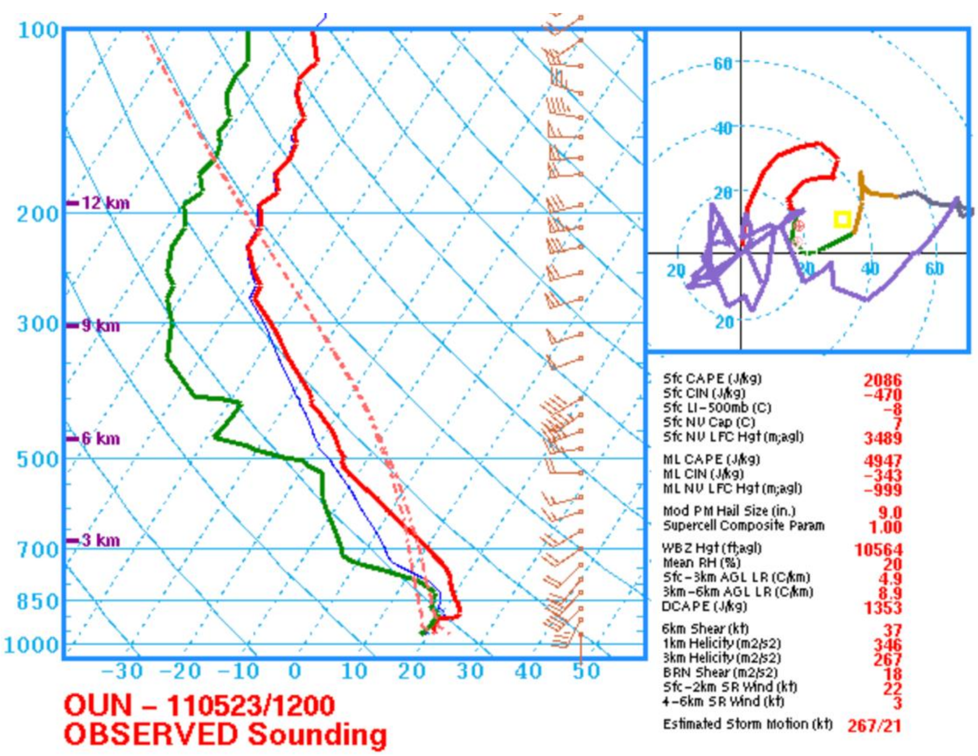

Figure 4.2: Sounding from OUN (Norman, OK) taken at 1200 UTC on 23 May 2011. Taken from the Storm Prediction Center's Severe Weather Archive.

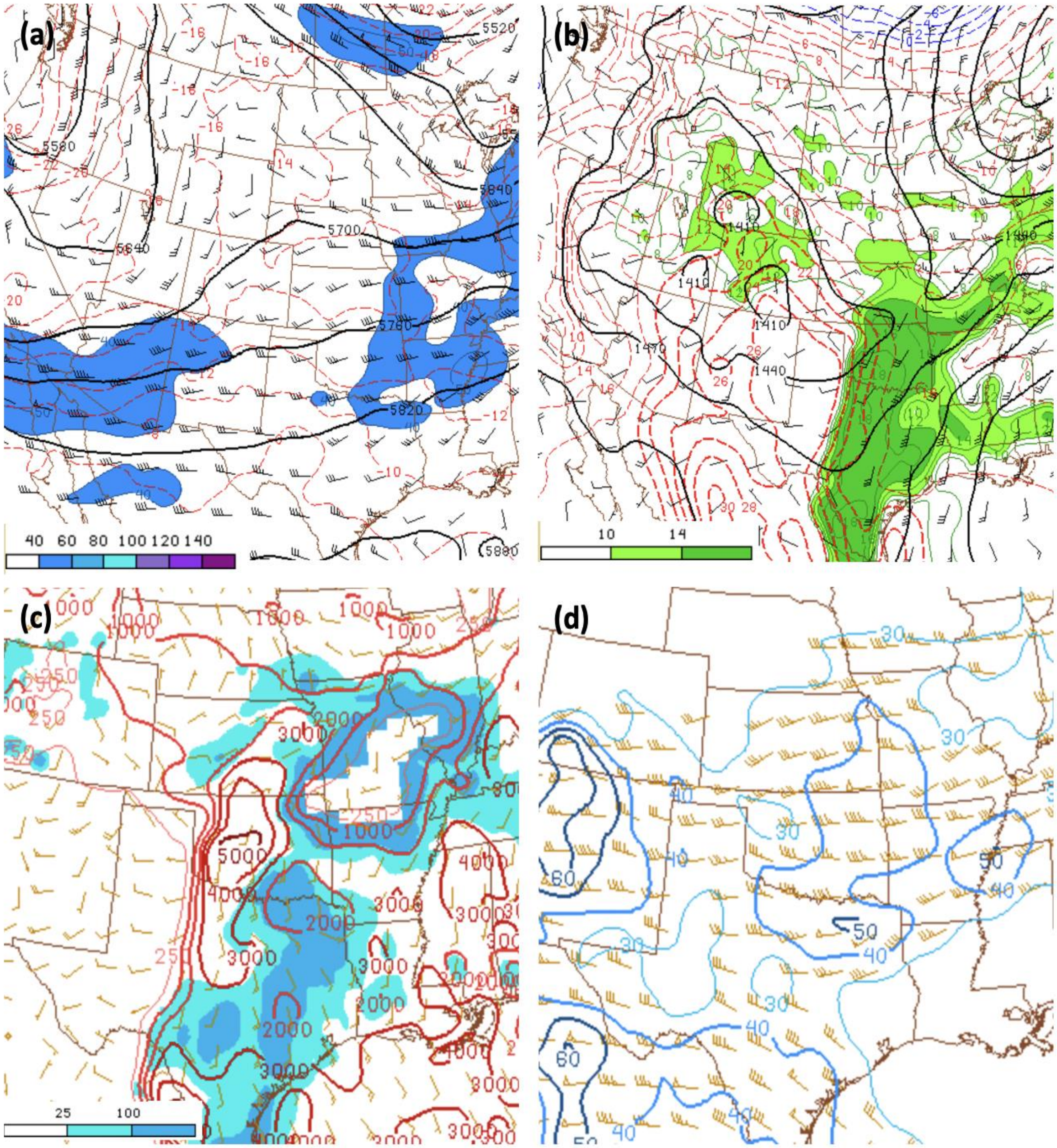

Figure 4.3: Overview of the synoptic environment on 23 May 2011. Showed above are: (a) 500 mb winds (kt) valid at 2000 UTC, b) 850 mb winds (kt) and moisture (°C) valid at 2000 UTC, (c) surface-based CAPE (red lines, J kg^{-1}) and CIN (fill, J kg^{-1}) valid at 2000 UTC, (d) 0 – 6 km bulk shear (contours, kt) and storm motion (wind barbs, kt) valid at 2000 UTC. Adapted from the Storm Prediction Center Mesoanalysis Archive.

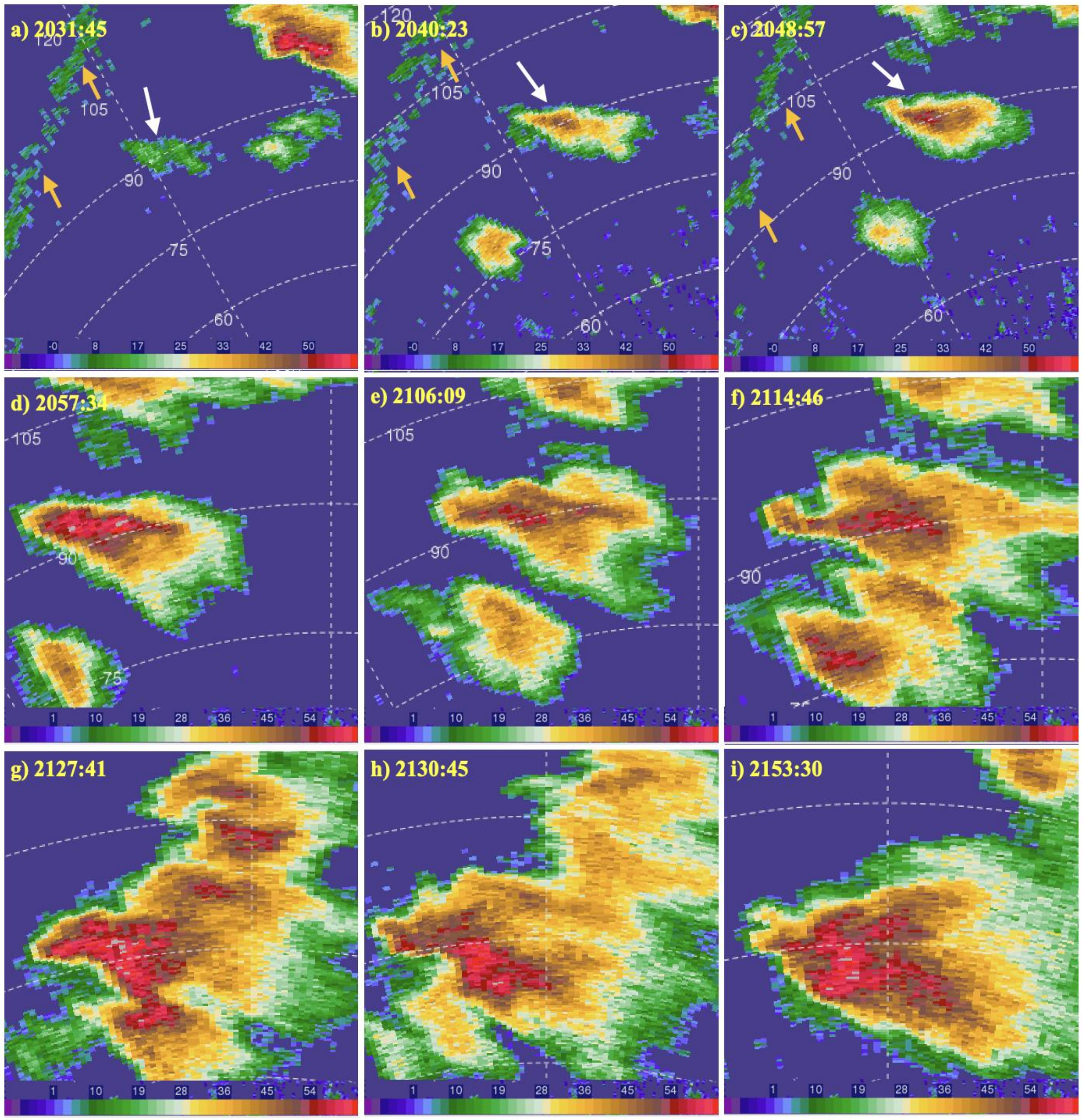

Figure 4.4: Formation of the 23 May 2011 hailstorm using 0.5° reflectivity data from the KFDR radar starting at 2031:45 UTC. Panel (a) shows the initial radar echo relative to the dryline, with the cell highlighted by a white arrow. Panels (b) and (c) show the formation of cell approximately ten minutes apart. Panels (d) through (i) zoom in on the main cell showing the cell's intensification. The color bar was increased to a maximum of 65 dB*Z* in panels (d) through (i) to account for increasing intensity. The white and orange arrows in panel (a) through (c) show the cell and the dryline, respectively.

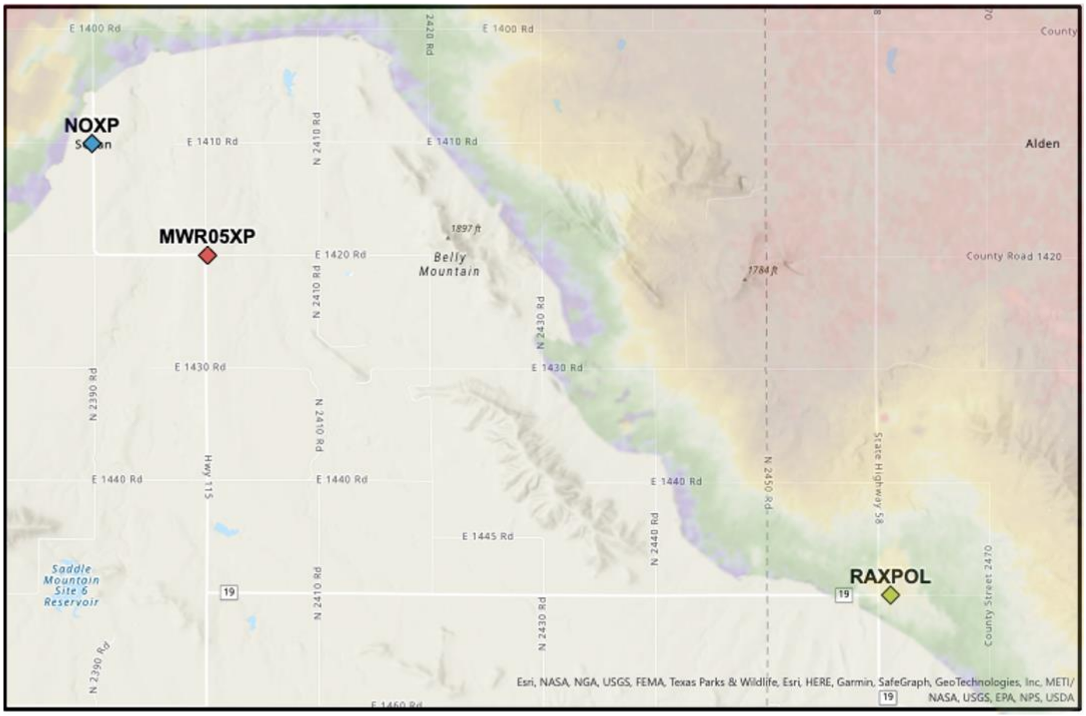

Figure 4.5: Mobile radar deployment map for 23 May 2011. The hook echo is located northwest of NOXP. Map created in ArcGIS by author.

thermodynamic environment for supercell development, with the most significant threats being large hail and possible tornadoes.

4.2 Supercell Formation

Around 2000 UTC, cells began forming east of the dryline, near Elk City, OK. Given the unstable environment, these cells rapidly developed into strong storms. The storm that would become the significant hailstorm appeared on radar at 2031 UTC, roughly 90 km northwest of KFDR (Figure 4.4a). After approximately 40 minutes, the storm started to develop supercell characteristics with an appendage forming and reflectivity values upwards of 60 dB*Z* (Figure 4.4f). At 2114 UTC, the supercell began merging with the weaker cells to its southwest and northeast. This storm underwent mergers for approximately half an hour. After the mergers, the storm intensified with the high reflectivity core increasing in size.

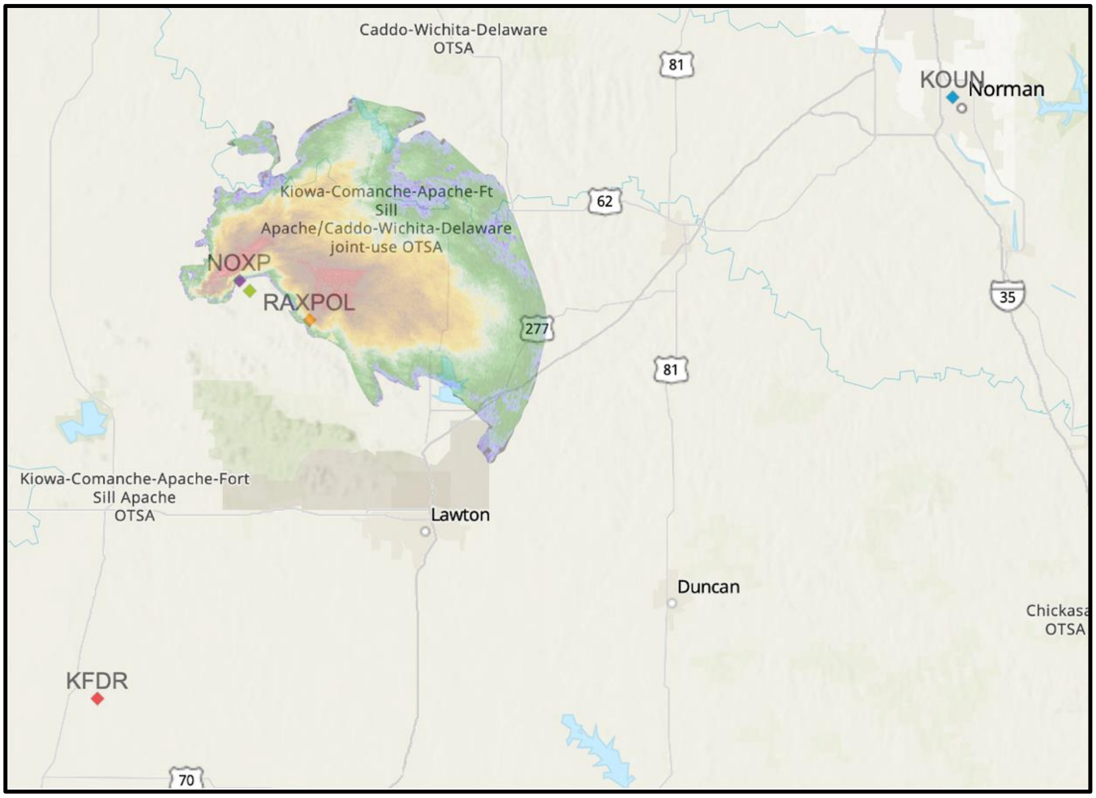

Figure 4.6: Locations of all five radars at approximately 2310 UTC. Basemap shows locations of nearby OTSAs (Oklahoma Tribal Statistical Areas). Map created in ArcGIS by author.

4.2.1 Radar Observations Times and Locations

KFDR observed the first echo of the storm at 2106 UTC and scanned the storm until 2359 UTC as it neared the end of its lifecycle. During this two-hour duration, the storm was observed by multiple radars. The locations of the three mobile radars are depicted in Figure 4.5, with all three located within 5 km of the storm. The storm's hook echo is located off the map, northwest of NOXP. Despite their proximity, the mobile radars had minimal coordination, resulting in their being located approximately along the same baseline. The S-band radars, KFDR and KOUN, were

Table 4.1: Starting and ending times of radar observations

Radar	Start time	End time
KFDR[3]	20:31:45 UTC	23:59:34 UTC
KOUN [3]	20:31:02 UTC	23:59:53 UTC
NOXP	22:36:20 UTC	23:15:17 UTC
MWR-05XP	23:04:02 UTC	23:19:12 UTC
RaXPol	23:10:02 UTC	23:39:04 UTC

90 km and 130 km from the storm, respectively, as shown in Figure 4.6. Table 4.1 provides the scanning times for each radar. The storm's evolution will be documented sequentially from the perspective of the first observing radar and transitioning to the subsequent radars as they began scanning.

4.3 Storm Evolution

The HailSTONE field campaign began making hailstone observations at 2157 UTC, approximately 35 minutes before the first mobile radar started scanning. Hailstone observations were recorded to the nearest minute. If a hailstone observation occurred within the same minute as the radar's lowest elevation level scan, they would be documented in the figure. In instances where hailstones of different sizes overlap at about the same time, the largest hailstone was plotted. The hailstones are color-coded based on size ranges. A legend showing the distribution of hailstone sizes and corresponding colors is provided at the bottom of Figure 4.7.

[3] KFDR and KOUN scanned and collected data throughout the day. Start and end times in the table depict the data collection period used in this study.

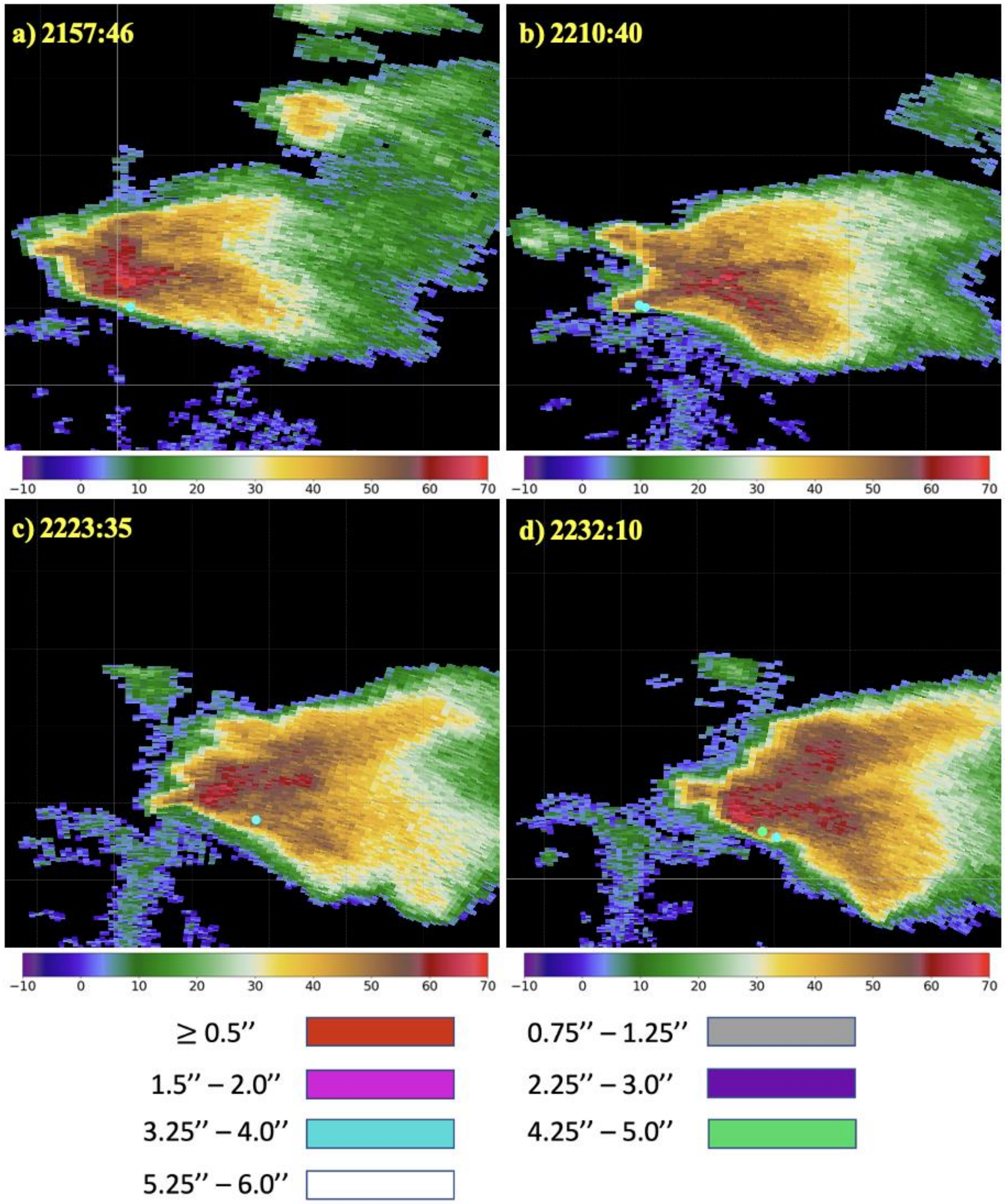

Figure 4.7: Evolution of the 23 May 2011 hailstorm using 0.5° reflectivity data from the KFDR radar starting at 2157:46 UTC. Panels (a) through (d) show the evolution of the supercell every 10 to 12 minutes. The cyan dots in panels (a) through (d) mark the location of observed hailstones from the HailSTONE field campaign. The hailstone size range and corresponding colors are depicted at the bottom of the figure. The hailstone legend will correspond to all future radar images.

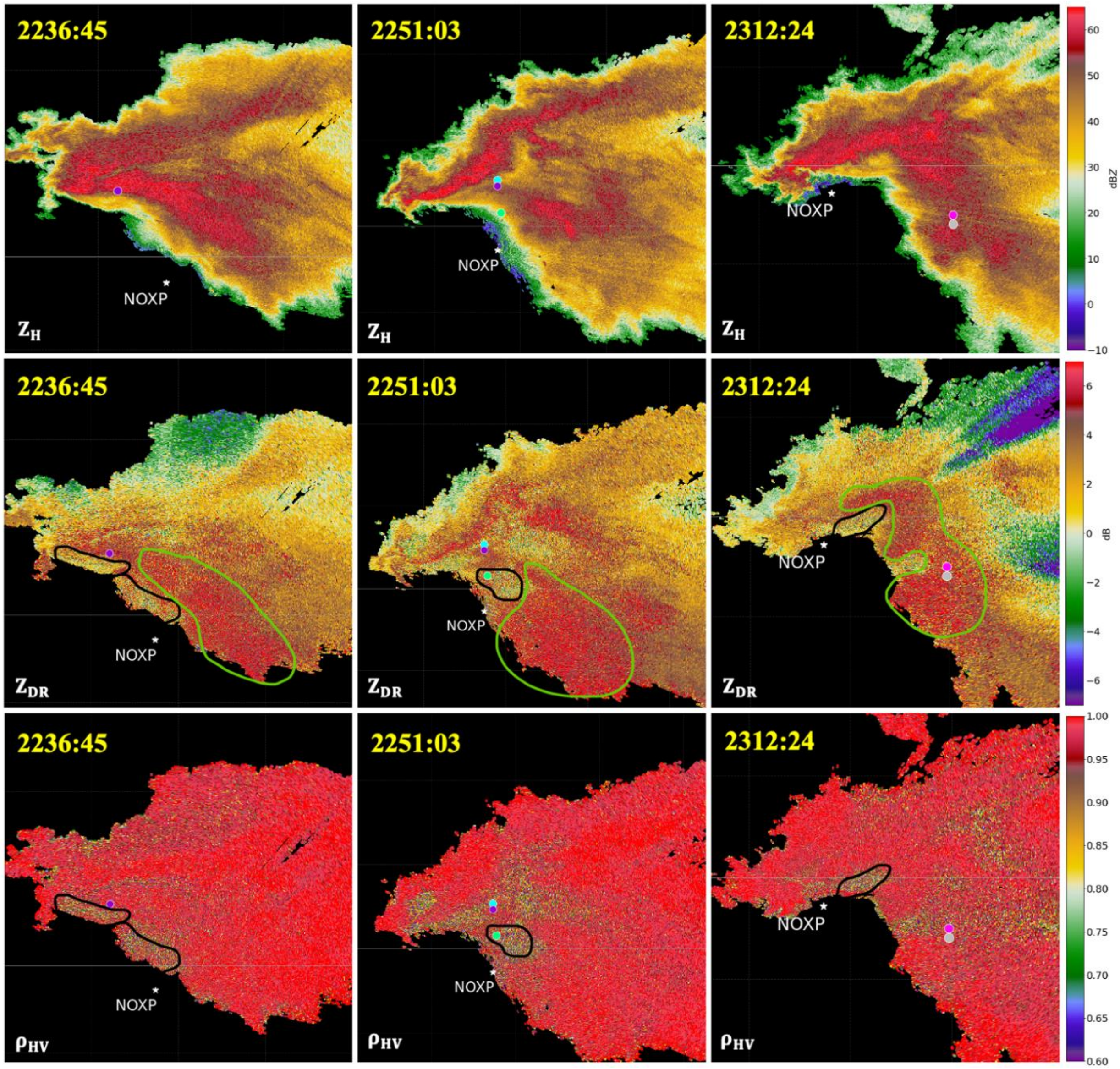

Figure 4.8: Evolution of the 23 May 2011 hailstorm using 2.0° polarimetric data from NOXP starting at 2236:45 UTC. Each column shows three different observation times approximately, 15 minutes apart. Each row displays a different polarimetric variable, starting with attenuation- corrected reflectivity and differential reflectivity, followed by cross-correlation coefficient, and specific differential phase. Areas circled in black indicate wet hail or heavy rain. Areas outlined in green show regions of enhanced Z_{DR} and K_{DP}.

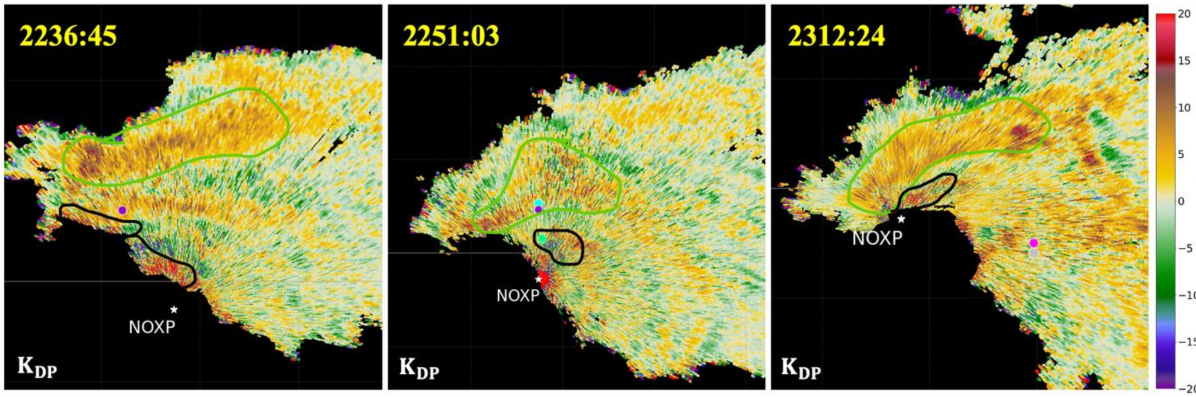

Figure 4.8 (continued)

The continuation of the supercell's evolution is shown in Figure 4.7, which displays data from KFDR from 2157 UTC to 2232 UTC. Each panel displays data at 12-minute intervals showing reflectivity at 0.5° elevation. Across all four observation times, hailstones measured between 3.25 in (8.3 cm) and 4.0 in (10.2 cm) were documented. In panel (d), a larger hailstone was observed, measuring between 4.25 in (10.8 cm) and 5.0 in (12.7 cm) . During this period, the formation of a hook echo begins. In Figure 4.7d, the high reflectivity echo adopts a "V-shape", which also has been known as the "flying eagle" or "flying V" signature, with the apex marking the location of the updraft. This shape results from the updraft acting as an obstacle, forcing the air aloft to diverge around it. Towards the end of this observation period, the largest hailstone within this storm was recorded, measuring 6 in (15.24 cm) in diameter, and currently holds the record for the largest hailstone in Oklahoma at that time. Further details regarding this record-breaking hailstone will be discussed in Section 4.4.

Figure 4.8 illustrates the storm's evolution as observed by NOXP from 2236 to 2312 at the lowest elevation angle of 2.0°, approximately 0.3 km above radar level (ARL). Since NOXP is a polarimetric radar, four variables are shown: Z_H, Z_{DR}, ρ_{HV}, and K_{DP}. It should be noted that there was an error in the original K_{DP} field, which did not account for half of the range derivative, effectively displaying a two-way K_{DP}. To correct this issue, the K_{DP} field was divided by 2. The first column shows the initial time frame at 2236:45 UTC. The radar echo shape is similar to that seen in Figure 4.7(d), the “flying V” echo but at a higher resolution, revealing more structural details. Areas denoted by the black polygons indicate locations of wet hail. Wet hail is characterized by low ρ_{HV}, positive Z_{DR}, due to the stabilizing water torus, and positive K_{DP}, whereas dry hail is identified by low ρ_{HV}, low or near zero Z_{DR} and low or near zero K_{DP}. The marked areas are not all-encompassing but serve as examples of regions within the storm where these phenomena occur. The green outlines highlight enhanced areas of Z_{DR} and K_{DP}.

In the first column of Figure 4.8, the enhanced areas of Z_{DR} and K_{DP} aligned with the observations in Kumjian (2013b) as depicted in Figure 2.3, where the K_{DP} foot is slightly offset from the Z_{DR} arc. As we move forward in time to the next two columns, the shapes of these polarimetric signatures change but remain in the same area of the storm. Throughout the storm’s evolution from the viewpoint of NOXP at 2.0°, the areas of wet hail occurred on the forward flank of the supercell near the radar. It should be noted that all the speckled areas of ρ_{HV} could contain hail, but it is unclear if it is wet hail or dry hail, possibly indicating mixed-phase precipitation. Six hailstones are documented in the radar images for the three observation times. The largest hailstone, measuring 5 inches, is indicated by the green dot in the second column of figures. This hailstone corresponds to one of the areas of wet hail observed in the radar echoes.

Figure 4.9 shows the same evolution as Figure 4.8 but at 15° in elevation, approximately 2.5 km ARL. Aloft, the presence of a LRR appears at 2314:54 UTC. In the first column, an area of high Z_{DR}, low ρ_{HV} and negative K_{DP} occurs near the radar. This area then grows in the next column, with the most notable change being the alternating pattern in the K_{DP} panel, where values shift from 10 degkm^{-1} to -10 degkm^{-1}. As the supercell begins to develop a longer appendage, seen in the third column of Figure 4.9, the pattern of positive than negative K_{DP} remains but moves

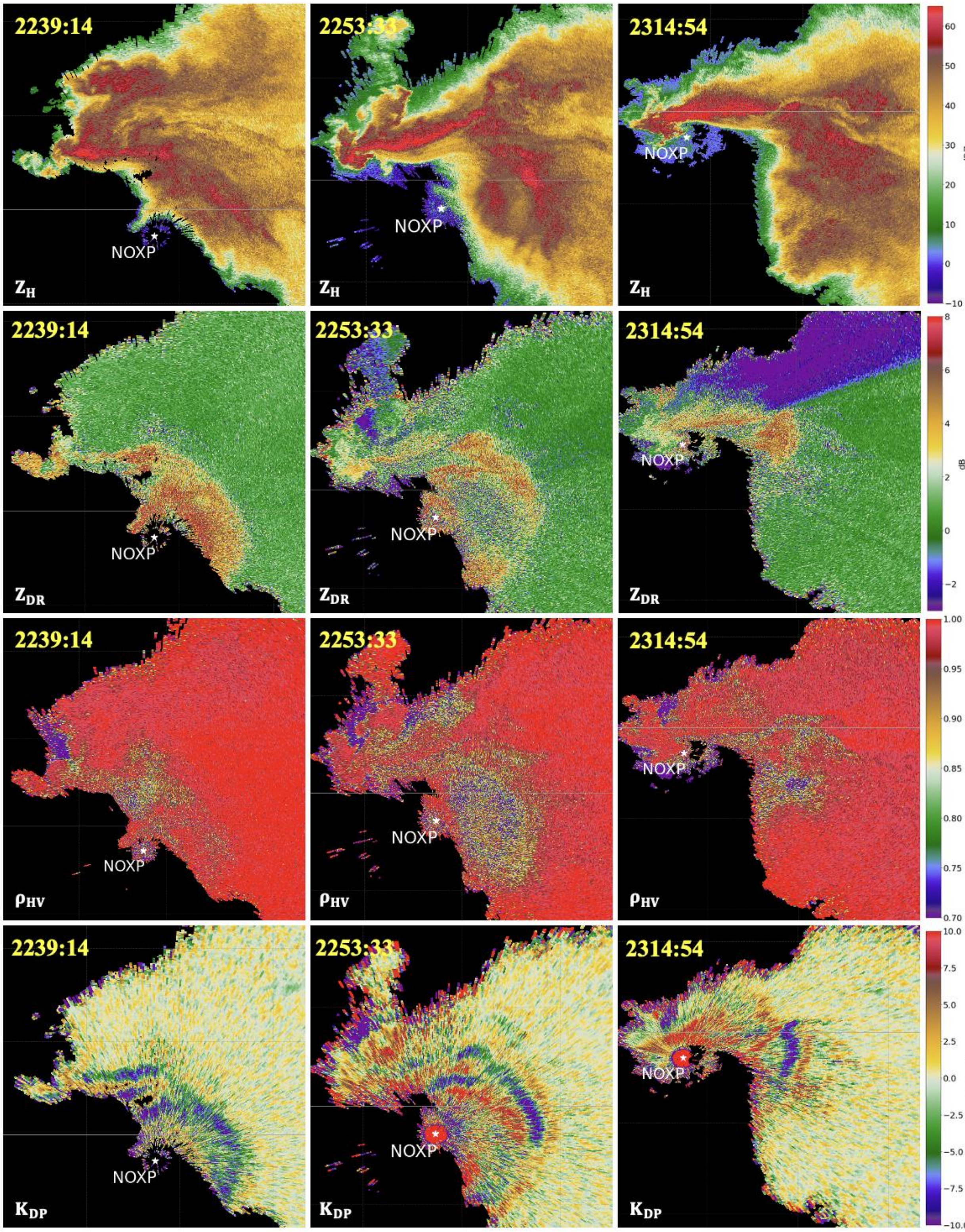

Figure 4.9: Same as above but at 15° in elevation.

to the forward flank fo the supercell, adjacent to the radar. Throughout the evolution, the areas of Z_{DR} , ρ_{HV} and K_{DP} increase and decrease in size, likely due to hail descending to the surface. Unfortunately, the radar did not scan high enough to observe the environmental freezing level, so 15° is still considered to be in the low levels of the supercell.

Figure 4.10 shows the storm's evolution observed by MWR-05XP in the next time steps. MWR-05XP scanned the storm for 15 minutes. As a result, the time of the first panel is slightly earlier than the last panel from NOXP. Since MWR-05XP is a conventional radar, only radar reflectivity is plotted. Each panel is plotted 6 to 8 minutes apart, starting at 2304:25 UTC. MWR-05XP utilized the STF-E scanning strategy, discussed in Section 3.1.3. Owing to this scanning strategy, the reflectivity values were lower than those observed by NOXP, RaXPol, and the NEXRAD radars. The color bar range was reduced by 20 dB*Z*, to identify any polarimetric signatures. In the first column of Figure 4.10, the LRR is visible at 2.0° and 16°. In the subsequent time steps, the storm develops a weak echo hole (WEH), as depicted in 2317:54 at 16°. Although hailstone observations were collected, none are marked on this figure, as they were not collected in the hook echo or storm appendage.

Figure 4.11 shows the storm's evolution observed by RaXPol starting at 2312:06 UTC. RaXPol began scanning 10 minutes before MWR-05XP stopped and continued for 20 minutes after MWR-05XP finished scanning. The first two column times overlap with those of MWR-05XP. However, since MWR-05XP is a conventional radar, the polarimetric variables from RaXPol's perspective are plotted. The first column of Figure 4.11 shows the supercell with two separate cores of high reflectivity values greater than 50 dB*Z*, separated by a low reflectivity area. Since Z_H and Z_{DR} were corrected for attenuation, the LRR is harder to identify. Another notable observation is the extensive areas of low ρ_{HV} throughout the supercell. These areas of low ρ_{HV}

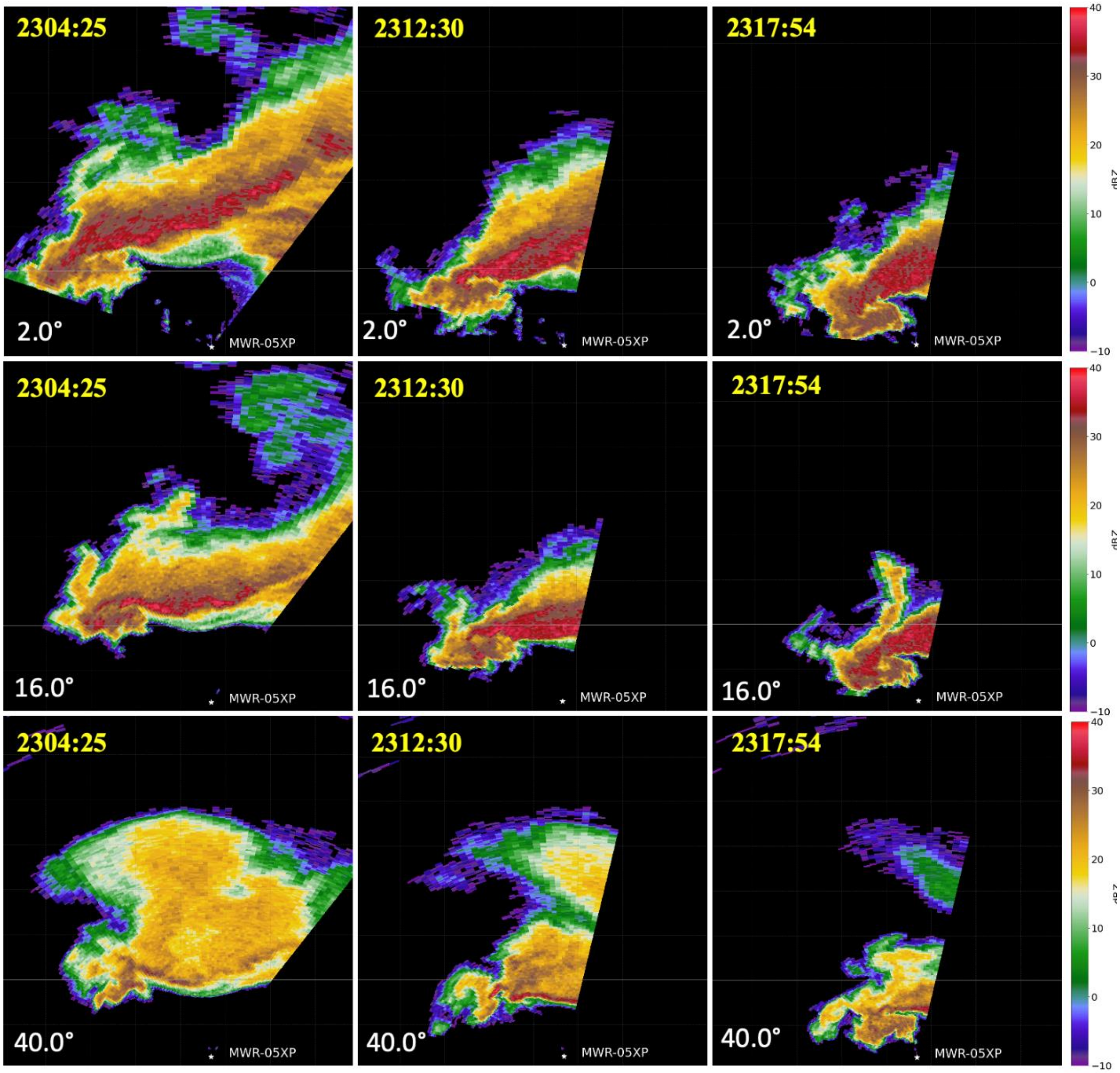

Figure 4.10: Continuation of the evolution of the 23 May 2011 hailstorm using 2.0°, 16.0°, and 40.0° elevation reflectivity data from MWR-05XP starting at 22304:25 UTC. Each column shows three different time steps approximately 8 minutes apart.

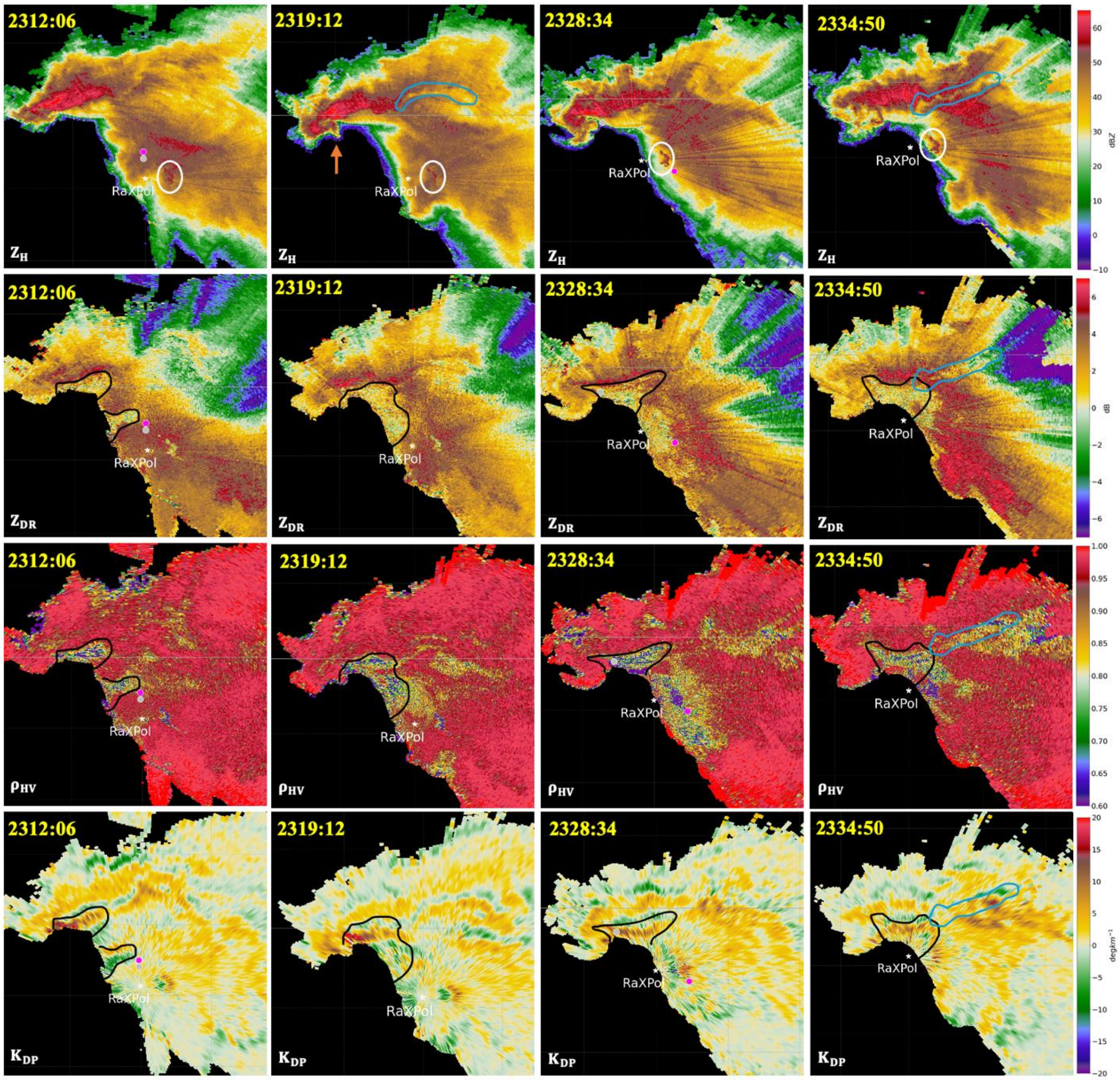

Figure 4.11: Evolution of the 23 May 2011 hailstorm using 2.0° polarimetric data from RaXPol starting at 2312:06 UTC. Each column shows four different time steps approximately 10 to 12 minutes apart. Each row displays a different polarimetric variable, starting with attenuation corrected reflectivity and differential reflectivity, followed by cross-correlation coefficient and specific differential phase. Areas circled in black indicate regions of wet hail. The areas marked in blue show the locations of the LRR. The white ellipse shows the location of a radar artifact in the data. The orange arrow indicates the location of a hammerhead signature in reflectivity. Observed hailstones from the HailSTONE field campaign are also marked in the figure.

Figure 4.12: Photograph of the 23 May 2011 hailstorm at approximately 2315 UTC. Photograph taken by Jeff Snyder.

correlate with regions of high and low Z_{DR}, and alternating areas of positive and near zero or slightly negative K_{DP}. Two locations circled in black indicate wet hail. As time progresses, the LRR becomes more apparent, with areas of wet hail remaining in the forward flanking region of the supercell northwest of the radar. Since the wet hail signature occurred close to the edge of the supercell which could indicate sparse hail fallout. A hammerhead signature appears in the hook echo, caused by the gust front wrapping up the hook echo. Four hailstones were documented in radar images for these timestamps: two at 2312 UTC and two at 2328 UTC. These stones are smaller than others documented in this study, with the maximum stone size being 2 in (5.1 cm). Figure 4.12 shows a photograph of the supercell at approximately 2315 UTC from the RaXPol deployment site.

At 16.0° the LRR becomes clearer in all four panels (Figure 4.13). Similar features to those in Figure 4.9 are observed. In the first column, an area of high Z_{DR}, low ρ_{HV} and negative K_{DP} is

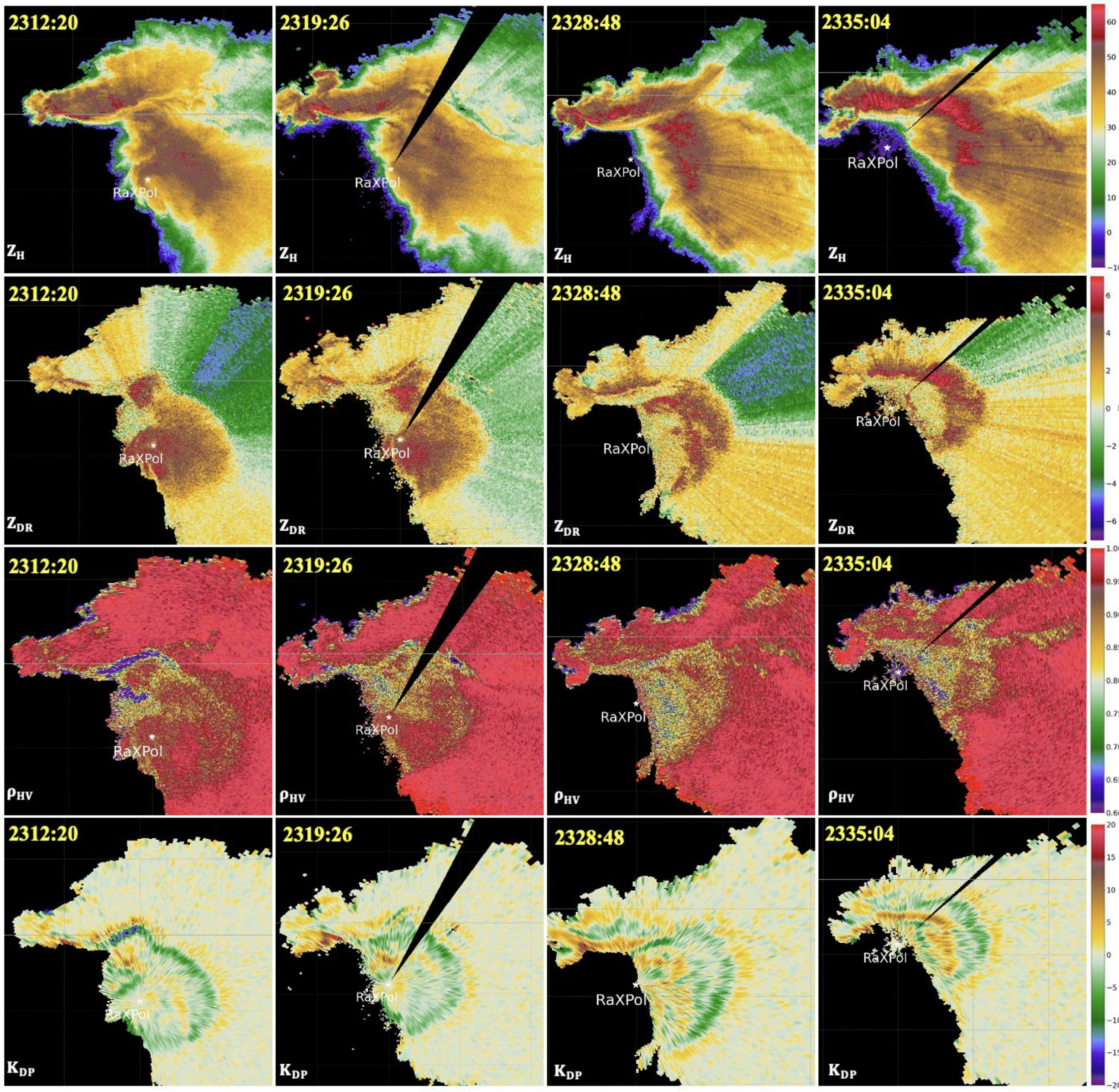

Figure 4.13: Same as above but at 15° in elevation.

evident near the radar. Also near the radar, areas of low ρ_{HV}, along with areas of high and low high Z_{DR} are seen. An alternating pattern in negative and positive is seen in K_{DP}. These areas remain roughly in the exact location but change in size, similar to Figure 4.9. A funnel cloud was observed and documented near the end of RaXPol's deployment. More details are discussed in Section 4.5. Figure 4.14 shows the next twenty minutes of the storm's evolution from the viewpoint of KOUN at 1.8° in elevation. KOUN has been collecting data throughout the duration of the storm evolution,

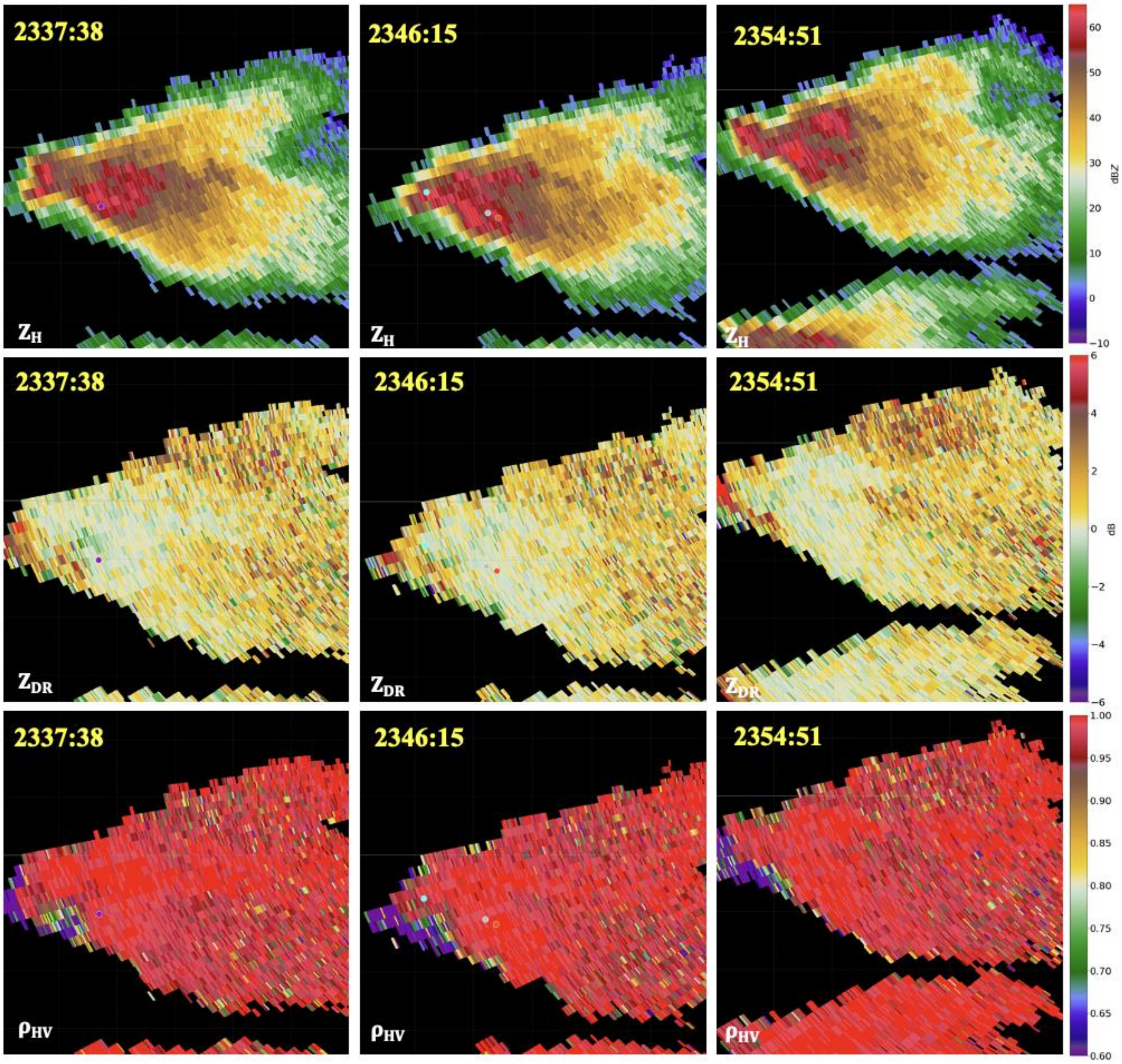

Figure 4.14: Continuation of the evolution of the 23 May 2011 hailstorm using 1.8° elevation data from KOUN starting at 2337:38 UTC. Each column shows three different time steps approximately 8 to 9 minutes apart. Each row displays a different polarimetric variable, starting with reflectivity, differential reflectivity, and cross-correlation coefficient. Observed hailstones from the HailSTONE field campaign are also marked in the figure.

and at this point, it is the only polarimetric radar collecting data. The first column shows an area of low ρ_{HV} and positive Z_{DR} near the storm's forward flank, corresponding to a hailstone

Figure 4.15: Photograph of the Oklahoma record hailstone collected by HailSTONE near Gotebo, OK.

observation marked by the purple dot. The next observation time includes three hailstone observations, all within the high-reflectivity core. In the last panel, no hailstone observations were reported. Another storm is seen south of the main supercell, suggesting that when both storms merged the primary cell dissipated.

4.4 The Oklahoma State Record Hailstone

At approximately 22:20 UTC, a hailstone measuring 6 in (15.24 cm) in diameter was recorded by the HailSTONE field campaign (Figure 4.15). This stone, which was observed near Gotebo, Oklahoma, became the largest recorded hailstone in Oklahoma. When the hailstone fell, two radars observed the storm: KFDR and KOUN. Figure 4.7 illustrates the storm observed by KFDR at the time of the hailstone's descent. Figure 4.16 shows the observations from KOUN near the time of the hailstone measurement. Since the supercell's distance was large, approximately 140

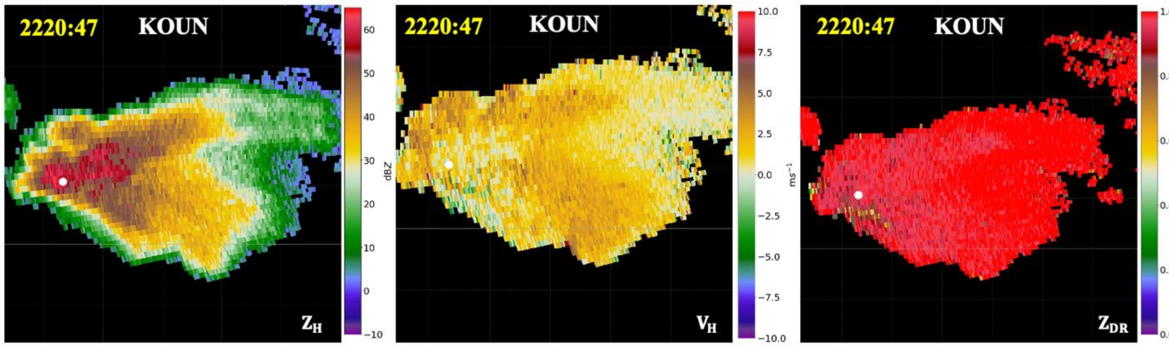

Figure 4.16: Radar observations from KOUN at 2220 UTC. The three panels show reflectivity, velocity, and differential reflectivity. The white dot marks the location of the giant hailstone.

km from KOUN, no clear details can be identified in the velocity and differential reflectivity plots, owing to the relatively coarse spatial resolution. The Z_{DR} color scale had to be adjusted to highlight any differences. Near where the hailstone fell, Z_{DR} drops to 0.6 dB. From the reflectivity panel in Figure 4.16, it is inferred that the hailstone fell near the updraft because the location of the marker is near the apex of the "flying V". A BWER was also visible aloft from KOUN at approximately 2222 UTC (Figure 2.6). The BWER is also indicative of a strong updraft, which would be needed for a stone of this size. This observation aligns with others in the literature, where larger hailstones are known to typically fall closer to the updraft, as smaller hailstones can be blown away by horizontal winds and the largest (and heaviest) hailstones' fall speeds tend to exceed that of the updraft closer to the core of the updraft.

4.5 Funnel-Cloud Vortex Signature

A vortex signature was indicated by RaXPol from 2335:53 UTC to 2338:49 UTC. Figure 4.17 shows the radar observations from RaXPol at 3.5° and 16.0° near the end of the visual funnel observation. The first row displays reflectivity, the black arrow indicating the location of the weak

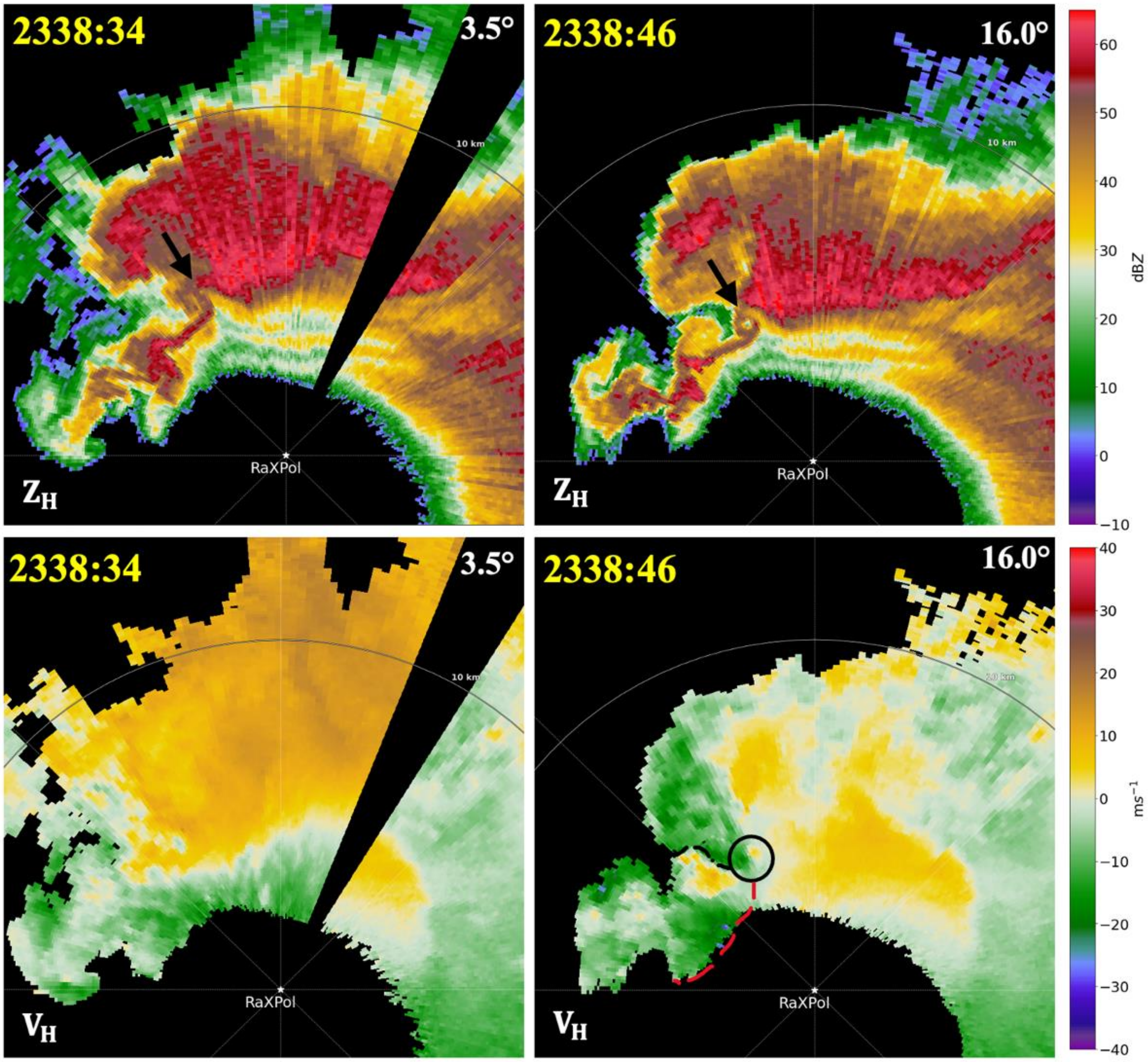

Figure 4.17: Radar observations of a funnel cloud vortex signature at 2338 UTC at 3.5° and 16.0° in elevation, observed by RaXPol. Four radar variables are displayed: reflectivity, radial velocity, differential reflectivity, and cross-correlation coefficient. The arrows display the location of the weak echo hole (WEH). The circles show the location of the cyclonic vortex signature. The dashed lines in the velocity plots show the locations of the rear flank gust front (RFGF) and a secondary internal surge.

echo hole (WEH). The second row shows velocity, where green represents flow towards the radar, and yellow represents flow away from the radar. The black circles denote the area of a cyclonic vortex signature. In the 16° velocity panel, the black line indicates the location of the rear flank

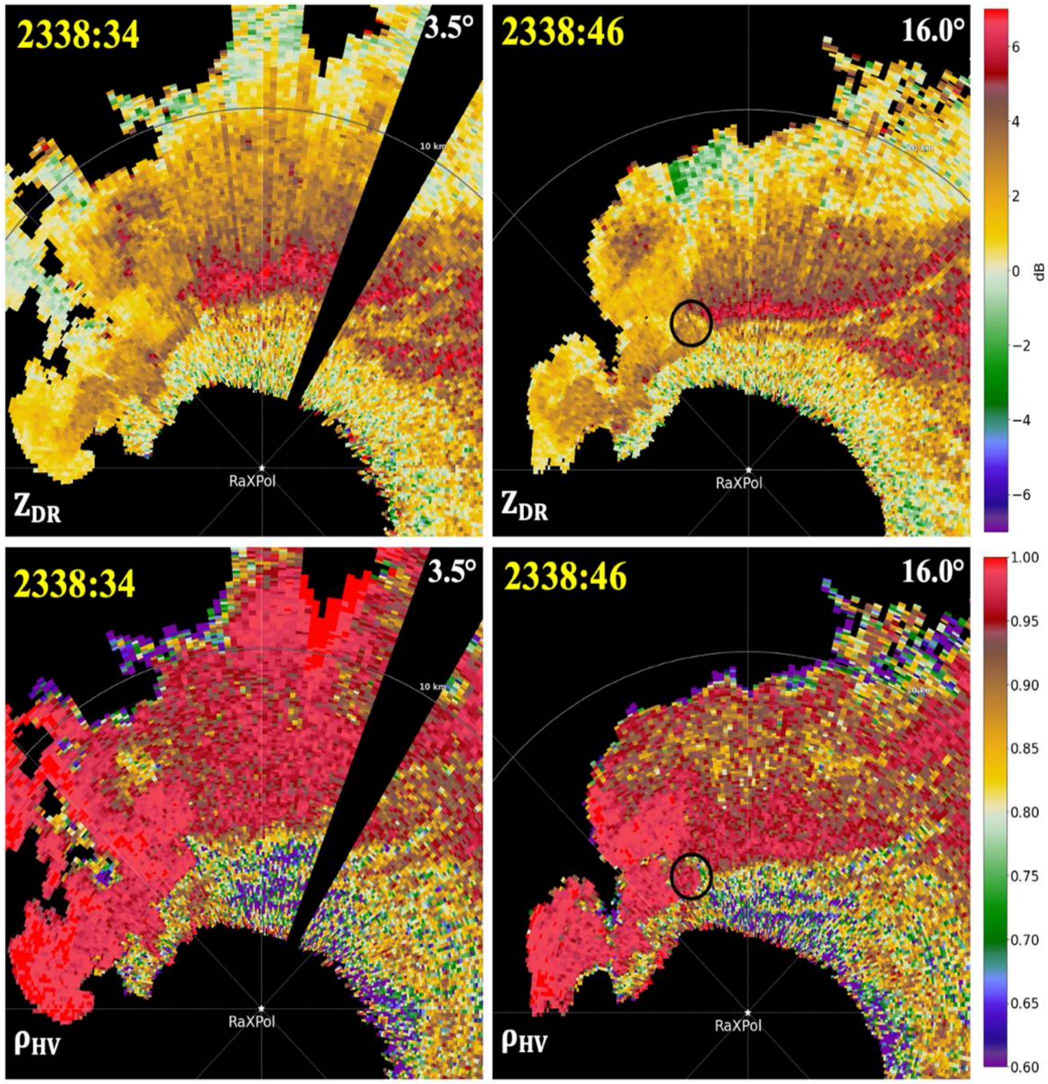

Figure 4.17 (continued)

gust front (RFGF), while the red lines show a secondary internal surge associated with the vortex formation. The WEH and cyclonic vortex signature are approximately 1.3 km ARL. It should be noted that the location of the vortex signature is northeast of the photographic location of the funnel in Figure 4.18. This is probably due to the large tilt of the funnel cloud. This funnel cloud was not observed by the nearby WSR-88D and was not tornado warned.

Figure 4.18: Photograph of highly tilted funnel cloud taken at approximately 2337 UTC, with a view to the west.

Chapter 5

Hailstorm Analysis

5.1 Comparison of Polarimetric Variables

There is a 5-minute period of overlap during which all five radars scanned the storm simultaneously. Among these, three radars are polarimetric. Figure 5.1 compares RaXPol, and NOXP at 23:12 UTC. Since NOXP is not a rapid scan radar, this is the only time frame that overlaps with the other radars. The first row compares reflectivity, where the mobile radars captured the hammerhead hook echo. The second row compares Z_{DR}. The black outline shows a good correspondence between the radars. These outlined areas display low Z_{DR}, surrounded by higher Z_{DR} values in excess of 4 dB. Differences in Z_{DR} between RaXPol and NOXP may be due to the applied attenuation correction. Although KOUN was scanning at this time, the storm was 135 km away, making it difficult to utilize to discern differences among the polarimetric variables.

The third row of Figure 5.1 illustrates the comparison between ρ_{HV}. The black outlines highlight areas of consistency across both radars. RaXPol exhibits a greater range of values, with the regions of low ρ_{HV} significantly lower than those in NOXP. The final row compares K_{DP}, with an arrow indicating the location of a large K_{DP} enhancement region of approximately 5 $\mathrm{deg km^{-1}}$. The black outline highlights another area of similar values that correlates with low ρ_{HV} values. From this comparison, we can conclude that although the NOXP polarimetric variables are not as clear as those from RaXPol, both polarimetric radars demonstrate good qualitative correspondence between the minimum and maximum values in the polarimetric variables.

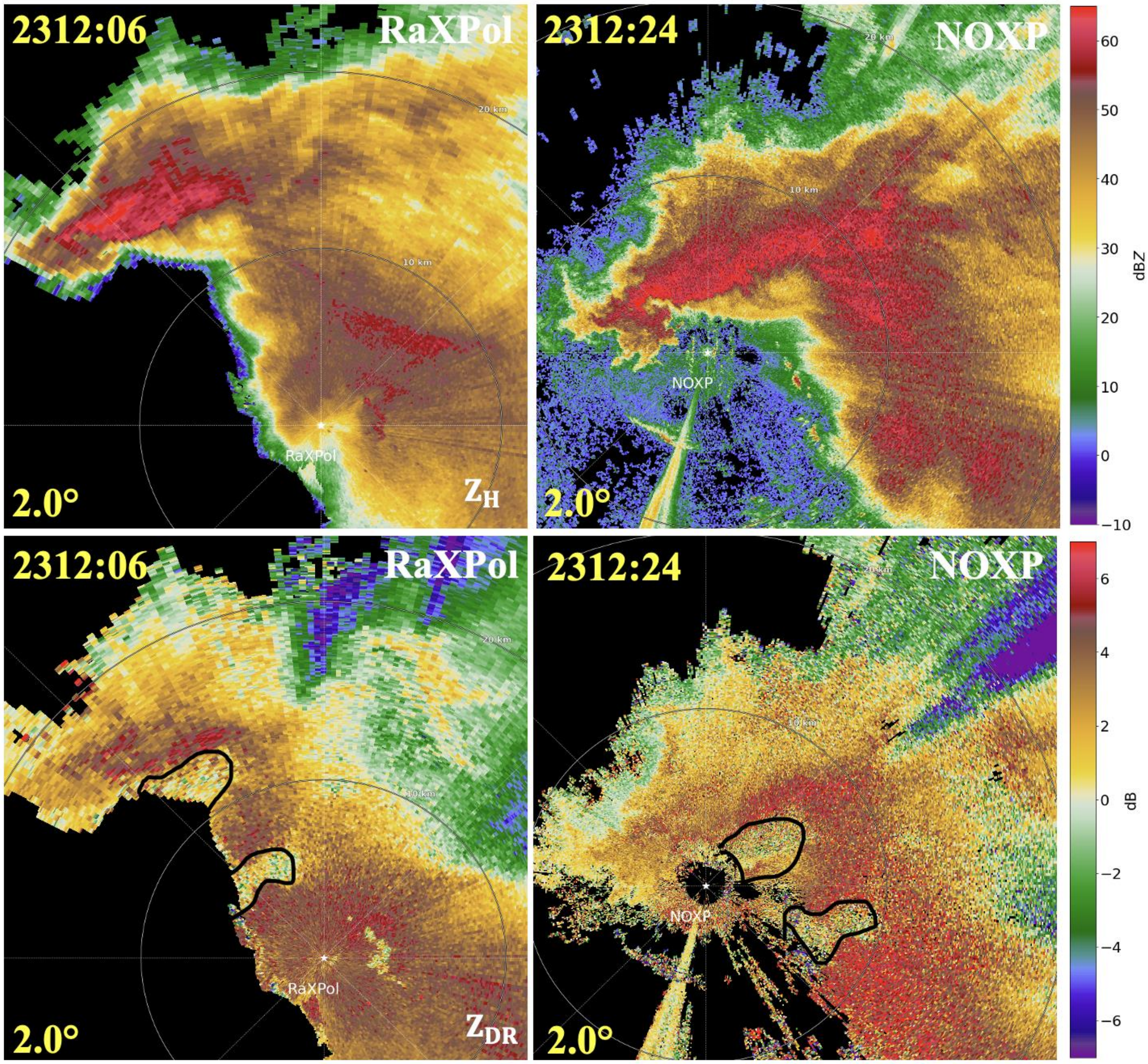

Figure 5.1: Comparison of polarimetric variables from RaXPol, and NOXP 2312 UTC. Black polygons show similarities across all radars for that variable.

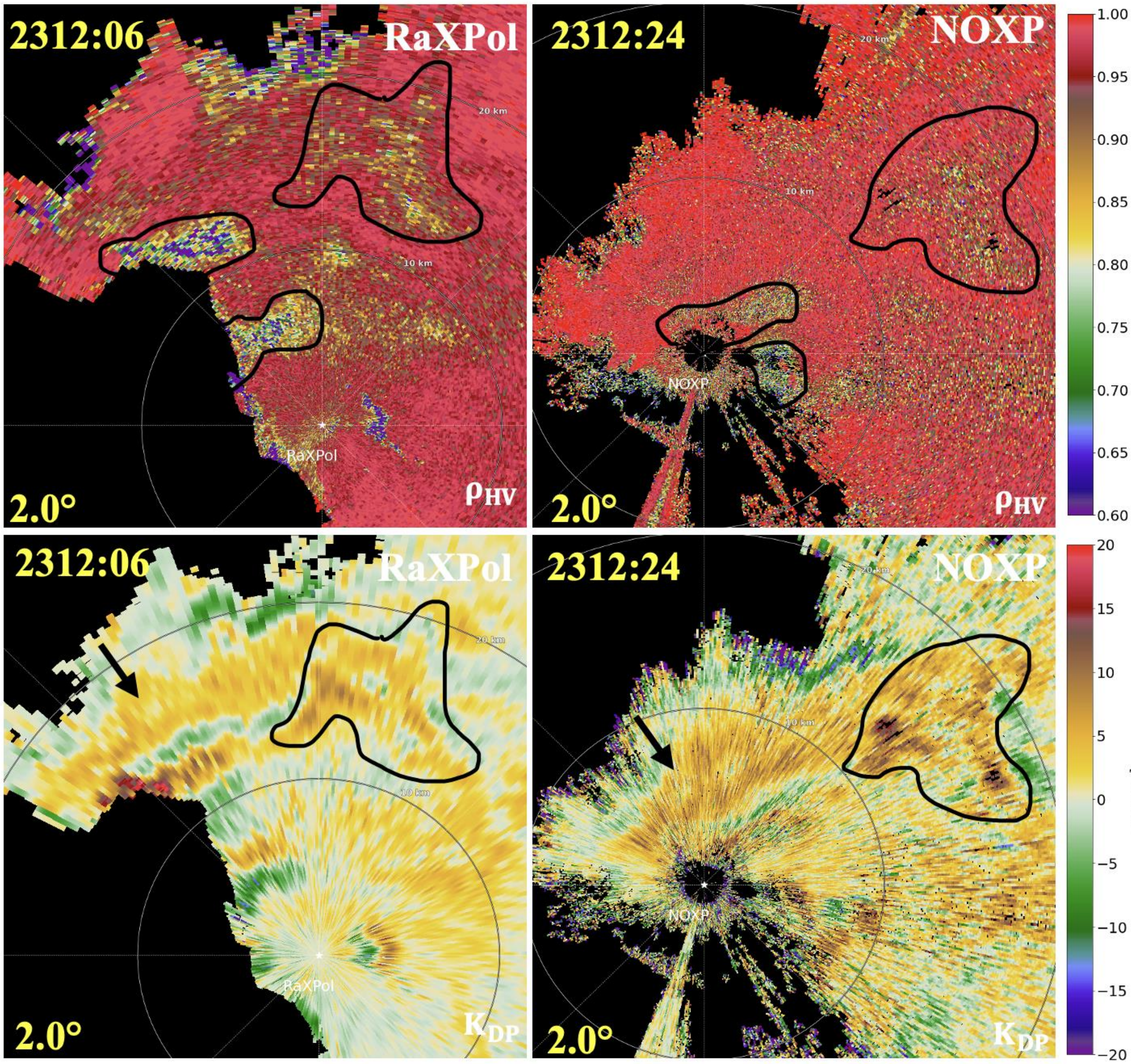

Figure 5.1 (continued)

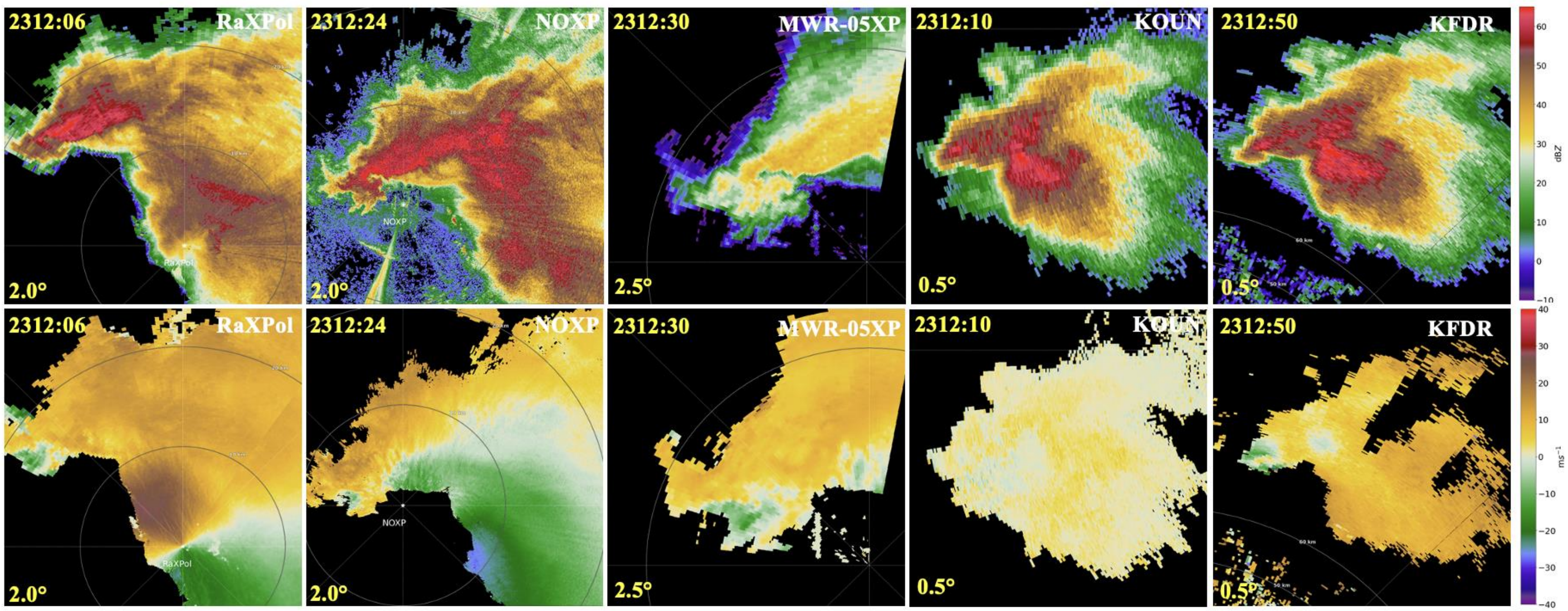

Figure 5.2: Comparison between all five radars at 2312 UTC. The top row displays reflectivity starting with the mobile radars, then the NEXRADs. The second row displays radial velocity in the same pattern.

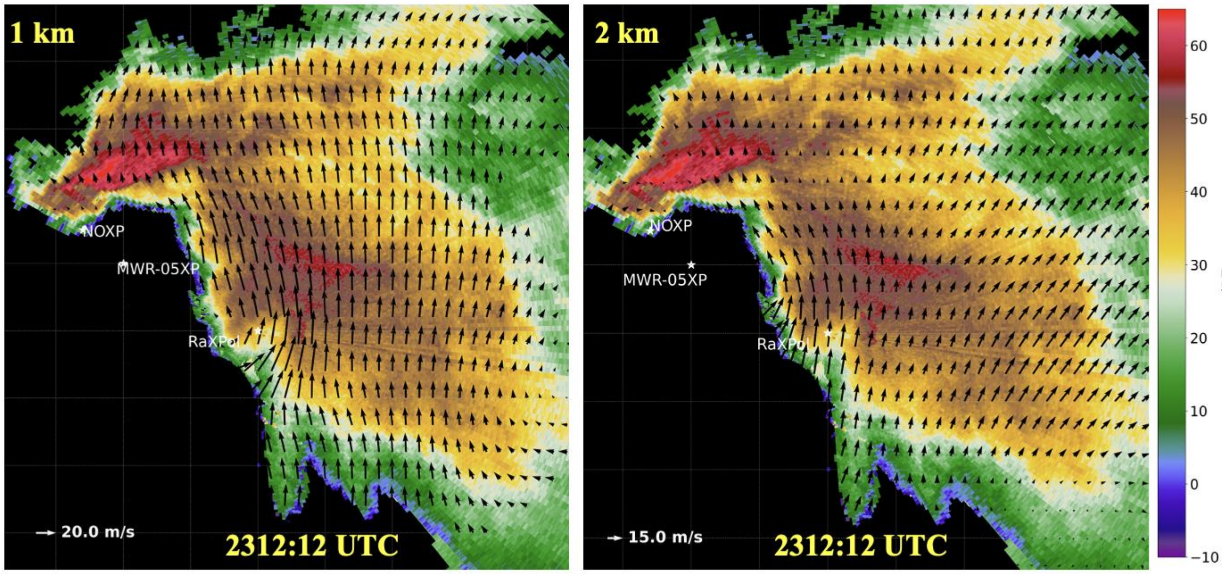

Figure 5.3: Multi-Doppler Analysis of the storm relative wind field from RaXPol, NOXP, and MWR-05XP at 1 km and 2 km.

5.2 Multiple-Doppler Analysis

Although the baseline between the mobile radars was suboptimal for retrieving the wind field near the hook echo, BWER, and regions of polarimetric debris signatures, a multi-Doppler analysis was conducted in an attempt to gain insight into the 3-D wind field. Using the SAMURAI variational analysis technique from LROSE, a multi-Doppler wind retrieval was done for the storm-relative wind field. Storm motion was calculated using FRACTL from LROSE, which is based on CEDRIC and REORDER. The storm speed of 6.1 ms^{-1} with a northeast direction of 36.15°. Figure 5.3 displays the results of the multi-Doppler analysis, centered on RaXPol. The overall wind field appears smooth. At 2 km, wind speeds throughout the supercell ranged from 15 ms^{-1} to 25 ms^{-1}. Figure 5.4 presents a zoomed-in portion of the multi-Doppler analysis, focusing on the hook echo. The scale was reduced to include slower wind speeds, allowing the quivers to

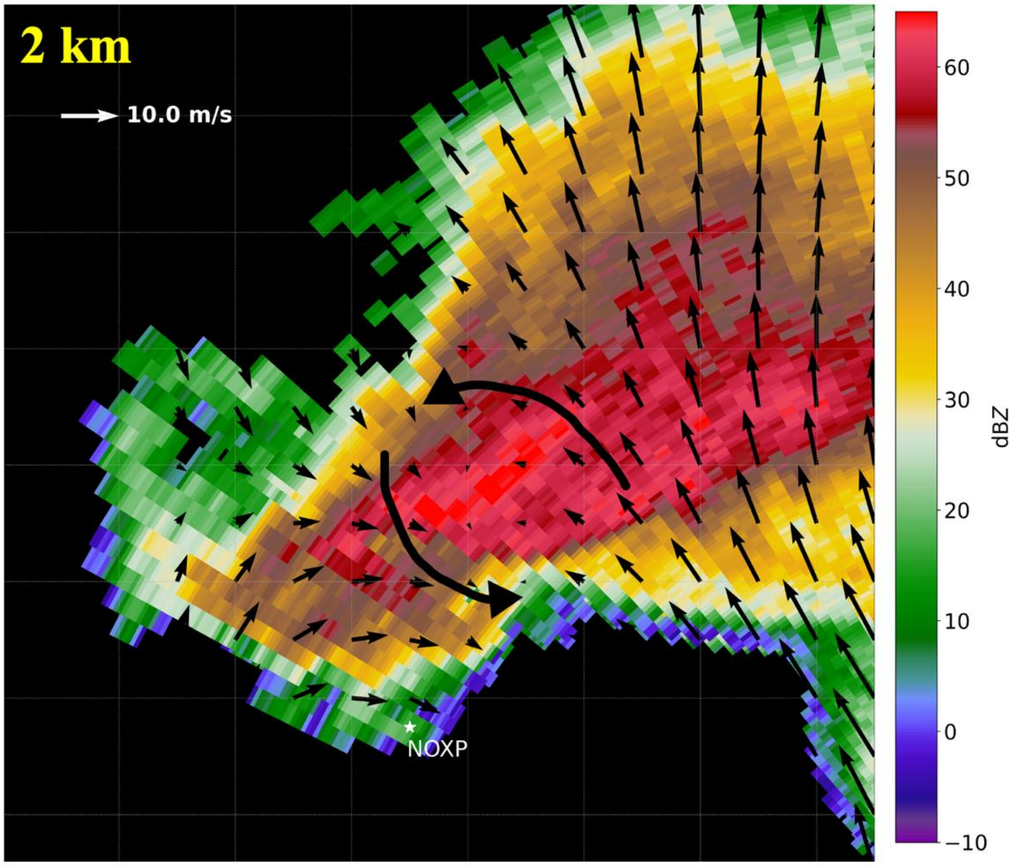

Figure 5.4: Same as the last figure but zoomed in to the hook echo. The quiver scale was reduced to visualize the winds in the hook echo. The black lines illustrate cyclonic rotation.

be visible in the hook echo. The broad cyclonic rotation occurred within the hook echo, which nearly went unnoticed owing to the higher wind speeds in the supercell. Due to the closeness of the mobile radars, the multi-Doppler analysis could only be done for the lowest 2.5 km of the storm before the cone of silence became too large. Unfortunately, this was the only multi-Doppler analysis that could be performed, as NOXP and MWR-05XP ceased recording shortly afterward. Owing to the long range of KOUN and KFDR from the storm, no multi-Doppler analysis was conducted using data from them.

5.4 Hydrometeor Classification

Since the hailstorm produced hail varying in size throughout its lifetime, a fuzzy logic hydrometeor classification algorithm (HCA) was used to determine the dominant hydrometeor type within areas of the storm. RadxPid, a function from LROSE, was used to create the three-dimensional fields of the NCAR particle identification (PID) (Vivekanandan et al. 1999). To use RadxPid, the 18z sounding launched from Norman, OK, (Figure 4.2) was used to provide a background profile. A provided X-band threshold file from LROSE was used, which has membership functions and weights specific to X-band. In the parameter file, K_{DP} and the attenuation-corrected fields for Z_H and Z_{DR} were used. A hydrometeor classification was done for RaXPol at 2.0° valid at 2312 UTC. However, the temperature profile used in the HCA resulted in inaccuracies, indicating that all the hydrometeors were in the ice phase at low-levels. The invalid temperature profile caused the HCA to fail and will be corrected in future work.

Chapter 6

Summary and Conclusions

On 23 May 2011, a prolific hailstorm formed in southwestern Oklahoma, producing a record-breaking hailstone that measured 6 in (15.24 cm) in diameter. This supercell, observed by five radars throughout its lifetime and eventual decay, included three X-band mobile radars: RaXPol, NOXP, and MWR-05XP. The other two radars were WSR-88Ds radars KFDR and KOUN. Among these, RaXPol, NOXP, and KOUN were polarimetric. This thesis aims to analyze the data collected by these radars and document the evolution of this historic hailstorm. The goal is to identify the features that evolved and changed throughout the storm's development and what this reveals about hail formation. The analyses focus on identifying the storm environment leading up to convective initiation and comparing polarimetric variables observed by different radar systems. This study also documents a funnel cloud observed near the end of the storm. By identifying features and behaviors that have been previously documented, this study aims to further credibility of their role and evolution in hailstorms.

Over the storm's 3-hour life, the supercell underwent numerous changes. The storm formed at approximately 2130 UTC and was initially observed by KFDR. Starting as an isolated cell, it intensified with high reflectivity values upwards of 50 dB*Z*, approximately 30 minutes post-formation. The storm underwent various mergers with nearby cells, eventually developing into an isolated supercell with the characteristic "flying-V" shape. At 2220 UTC, approximately 1 hour after formation, the HailSTONE field campaign measured a 6-inch hailstone, setting a new state record. This hailstone fell near the updraft, identified as the apex of the "flying-V". Subsequently, NOXP began scanning the storm, providing high-resolution polarimetric radar data. With NOXP, the polarimetric signatures LRR, Z_{DR} arc, and K_{DP} foot were observed. As the supercell changed shape and developed an appendage, areas of reduced ρ_{HV} indicated a decrease in homogeneity within the supercell. Low ρ_{HV} values, along with enhanced and reduced regions of Z_{DR} and K_{DP}, indicate the presence of wet and dry hail. Due to NOXP's relatively long 3-minute volumetric update, discerning the evolution of the polarimetric variables was challenging, but it can be concluded that wet hail occurred in the forward flank of the supercell.

As the supercell developed well-defined supercell characteristics, including a hook echo, MWR-05XP began scanning the storm. Although MWR-05XP is not polarimetric, its hybrid phased array technology enabled rapid updates within the storm. Despite low reflectivity values, due to the STF-E scanning strategy, the LRR and a WEH at 16.0° were clearly visible. Around this time, RaXPol also began scanning the storm. RaXPol's rapid scanning capability, allowed for detailed observation of the polarimetric variable evolution. Consistent with previous MWR-05XP scans, the LRR was present despite diminished resolution due to attenuation correction. Reduced ρ_{HV} values, along with regions of positive Z_{DR} and K_{DP}, indicated areas of wet hail. Throughout the storm's evolution, RaXPol detects large areas of reduced ρ_{HV} at 16.0°, with alternating areas of positive and near zero Z_{DR} and K_{DP}, indicating areas of hail fall.

Near the end of RaXPol's deployment, a funnel cloud developed and was observed by the radar. The funnel cloud was associated with a secondary internal surge and RFGF. A clear WEH was seen aloft at 16.0°, and a cyclonic vortex couplet was seen in the velocity data, indicating rotation. Throughout the storm's evolution, KOUN collected data approximately 140 km from the storm. Despite the long distance, polarimetric variables were available, although no distinct details were noted. During the storm's lifetime, 230 hailstones ranging from 0.25 inches to 6 inches in diameter were observed. The majority of large hailstones fell before 2300 UTC, with only a few being documented in this thesis. Based on the supercell's evolution, we can infer that this storm generated hail for the majority of its existence. The larger hailstones fell nearer to the updraft, while the smaller ones were observed in the forward flank of the supercell.

Multiple analyses were conducted including a comparative analysis of the radars and their variables, particularly polarimetric variables. There was a 5-minute period where the storm was sampled by all five radars. During this overlap, comparisons between RaXPol and NOXP's polarimetric variables showed good qualitative correspondence, with aligned areas of reduced ρ_{HV}. However, RaXPol displayed higher-quality radar returns, possibly due to resolution, wavelength differences, or the use of frequency hopping.

Reflectivity and velocity comparisons within the same minute across all five radars facilitated a multi-Doppler analysis of the mobile radars. The analysis revealed a smooth wind field throughout much of the supercell, with the storm motion being southeasterly. Due to the lack of upper elevation scans, the multi-Doppler wind retrieval extended only to 2.5 km. At 2 km, a broad circulation is observed in the hook echo. A fuzzy logic hydrometeor classification scheme was applied to discern the dominant hydrometeor type within the supercell. Due to issues with the conversion of the temperature file, the HCA provided invalid results. This issue will be corrected in future work.

This study provided an in-depth analysis of a historic storm. Despite the limited availability of mobile radar data during the observation of large hailstones, this study highlights the importance of future collaboration among mobile radars during field deployment. This dataset provided valuable insights into the behavior of the polarimetric variables, from the storm's growth to eventual decay. This research conducted an in-depth analysis of a historic storm. This study highlights the importance of future collaboration among mobile radars during field deployment due to the lack of mobile radar data collection during the storm's peak hail-producing period. The dataset provided valuable insights into the behavior of polarimetric variables, depicting the storm's growth and eventual decay. The researchers collected data on 230 hailstones during this storm, with some stones going unmeasured. An interesting finding was that the largest hailstones occurred approximately two hours after the formation of the storm cell. Notably, a strong updraft region was observed from KOUN indicating a BWER during the collection of the largest hailstones. Following this, the hailstones decreased in size, and approximately 1.5 hours later, a funnel cloud was observed while small hailstones were still being reported.

The storm probably produced large hail due to merging with other storms and absorbing the hail embryos from the flanking line. This hypothesis is supported by the timing of the BWER and strong updraft signatures two hours after formation. The majority of the hail occurred in the forward flank of the supercell which is due to the storm mergers. This case differs from other hailstorm cases for multiple reasons. One is an observable LRR that persisted for approximately 45 minutes, seen both at the surface and aloft. Another is the dynamic behavior of the polarimetric variables near RaXPol and NOXP, where the growth and shrinkage of areas occurred where hail was falling to the surface. hail falling to the surface. The funnel cloud exhibited a vortex signature with a WEH and cyclonic vortex signature aloft, but these features were not present at lower levels. There were not enough observations to know why the funnel cloud did not produce a tornado. This funnel cloud also was not tornado-warned. This could have occurred due to the horizontal structure of the funnel, only being vertical near the ground. The vertical part of the funnel cloud was located below the beam of the radar.

Finally, multiple opportunities for future work exist. The data collection of supercells and hailstorms has significantly increased in the last 13 years, with better coordination between mobile radars to mitigate the baseline issue. Similar qualitative analyses on additional cases can reveal similarities or differences to phenomena found in this study. Furthermore, vertical cross-sections and reconstructed RHIs of reflectivity and the polarimetric variables could provide deeper insights into their evolution. An updated fuzzy-logic HCA that reduces the reliance on reflectivity data could also be beneficial for identifying hail regions within supercells observed at X-band.

Reference List

Allen, J. T., I. M. Giammanco, M. R. Kumjian, H. Jurgen Punge, Q. Zhang, P. Groenemeijer, M. Kunz, and K. Ortega, 2020: Understanding Hail in the Earth System. *Reviews of Geophysics*, **58 (1)**, 1–49, https://doi.org/10.1029/2019RG000665.

Battaglia, A., S. Tanelli, S.Kobayashi,D. Zrnic,R. J.Hogan, andC. Simmer, 2010: Multiple-scattering in radar systems: A review. *J. Quant. Spectrosc. Radiat. Transfer*, **111**, 917–947.

Bell, M. M., M. T. Montgomery, and K. A. Emanuel, 2012: Air-sea enthalpy and momentum exchange at major hurricane wind speeds observed during CBLAST. *J. Atmos. Sci.*, **69**, 3197–3222, doi:10.1175/JAS-D-11-0276.1.

Blair, S. F., and Coauthors, 2017: High-resolution hail observations: Implications for NWS warning operations. *Weather and Forecasting*, **32 (**3), 1101-1119, https://doi.org/10.1175/WAF-D-16-0203.1.

Bluestein, H. B., M. M. French, I. PopStefanija, R. T. Bluth, and J. B. Knorr, 2010: A mobile, phased-array Doppler radar for the study of severe convective storms. *Bull. Amer. Meteor. Soc*., **91,** 579–600.

Bluestein, H. B., M. M. French, R. L. Tanamachi, S. Frasier, K. Hardwick, F. Junyent, and A. L. Pazmany, 2007: Close-range observations of tornadoes in supercells made with a dual-polarization, X-band, mobile Doppler radar. *Mon. Wea. Rev.,* **135**, 1522–1543.

Bluestein, H. B., C. C. Weiss, and A. L. Pazmany, 2004: The vertical structure of a tornado near Happy, Texas, on 5 May 2002: High-resolution, mobile, W-band, Doppler radar observations. *Mon. Wea. Rev.*, **132**, 2325–2337.

Bluestein, H. B., A. L. Pazmany, J. C. Galloway, and R. E. Mcintosh, 1995: Studies of the substructure of severe convective storms using a mobile 3-mm-wavelength Doppler radar. *Bull. Amer. Meteor. Soc.*, **76**, 2155–2169.

Bluestein, H. B., and W. P. Unruh, 1989: Observations of the wind field in tornadoes, funnel clouds, and wall clouds with a portable Doppler radar. *Bull. Amer. Meteor. Soc.*, **70,** 1514–1525.

Bringi, V. N., and V. Chandrasekar, 2001: Polarimetric Doppler Weather Radar. Principles and Applications. Cambridge University Press, 636 pp.

Carlin, J. T., and Ryzhkov, A. V., 2019: Estimation of melting-layer cooling rate from dual-polarization radar: Spectral bin model simulations. *J. Appl. Meteor. Climatol* **58**(7), 1485–1508. https://doi.org/10.1175/jamc-d-18-0343.1

Conway, J., and D. S. Zrnic, 1993: A Study of Embryo Production and Hail Growth Using Dual-Doppler and Multiparameter Radars. *Mon. Wea. Rev*, **121**, 2511–2528.

Dawson, D. T., E. R. Mansell, Y. Jung, L. J. Wicker, M. R. Kumjian, and M. Xue, 2014: Low-level ZDR signatures in supercell forward flanks: The role of size sort- ing and melting of hail. *J. Atmos. Sci*, **71 (1),** 276–299, https://doi.org/10.1175/JAS-D-13-0118.1.

DeHart, J., Dixon, M., Javornik, B., Bell, M., Cha, T.-Y., DesRosiers, A., & Lee, W.-C. 2024: nsf-lrose/lrose-releases:lrose-jade-20230814(lrose-jade-20230814).Zenodo. https://doi.org/10.5281/zenodo.11479603

Dennis, E. J., and M. R. Kumjian, 2017: The impact of vertical wind shear on hail growth in simulated supercells. *J. Atmos. Sci*, **74 (3)**, 641– 663, https://doi.org/10.1175/JAS-D-16-0066.1.

Doviak, R. J., and D. S. Zrnić, 1993: Doppler Radar and Weather Observations. 2nd ed. Dover Publications, Mineola, NY, 562 pp.

Faust, E., M. Bove, and A. Radler, 2022: Thunderstorms, hail, and tornadoes: Localized but extremely destructive. Thunderstorm, hail and tornado risks | Munich Re. Accessed 1 June 2024,https://www.munichre.com/en/risks/natural-disasters/thunderstorms-hail-tornados.html

Foote, G. B., 1984: A Study of Hail Growth Utilizing Observed Storm Conditions. *J. Appl. Meteor. Climatol.*, **23 (1),** 84–101, https://doi.org/10. 1175/1520-0450(1984)023(0084:ASOHGU) 2.0.CO;2,

Fujita, T., 1958: Mesoanalysis of the Illinois tornadoes of 9 April 1953. *J. Meteor.*, **15**, 288–296.

Griffin, C. B., C. C. Weiss, A. E. Reinhart, J. C. Snyder, H. B. Bluestein, J. Wurman, and K. A. Kosiba, 2018: In situ and radar observations of the low reflectivity ribbon in supercells during VORTEX2. *Mon. Wea. Rev.*, **146**, 307–327.

Gunturi, P., and M. K. Tippett, 2017: Managing severe thunderstorm risk: Impact of ENSO on U.S. tornado and hail frequencies. Willis Re, Minneapolis, MN, USA.

Helmus, J. J., and S. M. Collis, 2016: The Python ARM Radar Toolkit (Py-ART), a Library for Working with Weather Radar Data in the Python Programming Language. *Journal of Open Res. Software*, **4 (1),** 25, https://doi.org/10.5334/jors.119.

Heymsfield, A. J., 1982: A Comparative Study of the Rates of Development of Potential Graupel and Hail Embryos in High Plains Storms. *J. Atmos. Sci.*, **39 (12),** 2867–2897, https://doi.org/10.1175/1520-0469(1982)039⟨2867:ACSOTR⟩ 2.0.CO;2

Houser, J. L., H. B. Bluestein, and J. C. Snyder, 2016: A finescale radar examination of the tornadic debris signature and weak-echo reflectivity band associated with a large, violent tornado. *Mon. Wea. Rev*., **144**, 4101–4130.

Hubbert, J. C., V. N. Bringi, L. D. Carey, and S. Bolen, 1998: CSU-CHILL polarimetric radar measurements from a severe hail storm in eastern Colorado. *J. Appl. Meteor*., **37**, 749–775.

Hubbert, J. and V.N. Bringi, 1995: An Iterative Filtering Technique for the Analysis of Copolar Differential Phase and Dual-Frequency Radar Measurements. *J. Atmos. Oceanic Technol.,* **12**, 643–648.

Knight, C. A., D. H. Ehhalt, N. Roper, and N. C. Knight, 1975: Radial and Tangential Variation of Deuterium in Hailstones. *J. Atmos. Sci*, **32 (10),** 1990–2000, https://doi.org/10.1175/1520-0469(1975)032⟨1990:RATVOD⟩ 2.0.CO;2

Knight, C. A., and N. C. Knight, 1970: Hailstone Embryos. *J. Atmos. Sci.*, **27 (4)**, 659–666, https://doi.org/10.1175/1520-0469(1970)027⟨0659:HE⟩ 2.0.CO;2

Kumjian, M. R., 2013b: Principles and applications of dual-polarization weather radar. Part II: Warm and cold season applications. *J. Oper. Meteor*., **1 (20)**, 243–264,

Kumjian, M., 2013a: Principles and applications of dual-polarization weather radar. Part I: Description of the polarimetric radar variables. *J. Oper. Meteor*., **1 (19),** 226–242, https://doi.org/10.15191/nwajom.2013.0119.

Kumjian, M. R., and A. V. Ryzhkov, 2008: Polarimetric signatures in supercell thunderstorms. *J. Appl. Meteor. Climatol.*, **47 (7)**, 1940–1961, https://doi.org/10.1175/2007JAMC1874.1.

Lamb, D., and J. Verlinde, 2011: Physics and chemistry of clouds. Cambridge University Press, United Kingdom, https://doi.org/10.1017/CBO9780511976377.

Lemon, L. R., 1998: The radar ”three-body scatter spike”: An operational large- hail signature. *Wea. Forecasting*, **13 (2)**, 327–340, https://doi.org/10.1175/ 1520-0434(1998)013⟨0327:TRTBSS⟩2.0.CO;2.

Loeffler, S. D., Kumjian, M. R., Jurewicz, M., & French, M. M. 2020: Differentiating between tornadic and nontornadic supercells using polarimetric radar signatures of hydrometeor size sorting. Geophysical Research Letters, 47, https://doi.org/10.1029/2020GL088242

Maesaka, T., Iwanami, K. and Maki, M., 2012: Non-negative KDP Estimation by Monotone Increasing PHIDP Assumption below Melting Layer. *The Seventh European Conference on Radar in Meteorology and Hydrology*.

Nelson, S. P., 1983: The influence of storm flow structure on hail growth. 1965–1983 pp., https://doi.org/10.1175/1520-0469(1983)040⟨1965:TIOSFS⟩2.0.CO;2.

NOAA NSSL, 2024: Research Tools: Mobile Radar. Accessed 20 March 2024, https://www.nssl.noaa.gov/tools/radar/mobile/

Oye, R., C. Mueller, and S. Smith, 1995: Software for radar translation, visualization, editing, and interpolation. *27th Conf. on Radar Meteorology*, Vail, CO, Amer. Meteor. Soc., 359–361.

Pazmany, A. L., J. B. Mead, H. B. Bluestein, J. C. Snyder, and J. B. Houser, 2013: A mobile rapid-scanning X-band polarimetric (RaXPol) Doppler radar system. *J. Atmos. Oceanic Technol.*, **30**, 1398–1413.

Picca, J., and A. Ryzhkov, 2012: A dual-wavelength polarimetric analysis of the 16 May 2010 Oklahoma city extreme hailstorm. *Mon. Wea. Rev.*, **140 (4)**, 1385–1403, https://doi.org/10.1175/MWR-D-11-00112.1.

Rasmussen, R. M., and Heymsfield, 1987: Melting and shedding of graupel and hail. Part I: Model Physics. 2754–2763 pp.

Romine, G. S., D. W. Burgess, and R. B. Wilhelmson, 2008: A dual-polarization-radar-based assessment of the 8 May 2003 Oklahoma City area tornadic supercell. *Mon. Wea. Rev.*, **136**, 2849–2870

Ryzhkov, A. V., and Coauthors, 2007a: Comparison of polarimetric algorithms for hydrometeor classification at S and C bands. Preprints, *33rd Conf. on Radar Meteorology*, Cairns, Queensland, Australia, Amer. Meteor. Soc., 10.3.

Ryzhkov, A. V., T. J. Schuur, D. W. Burgess, and D. S. Zrnic, 2005: Polarimetric tornado detection. *J. Appl. Meteor*., **44,** 557–570.

Ryzhkov, A., D. Burgess, D. Zrnic, T. Smith, and S. Giangrande, 2002: Polarimetric analysis of a 3 May 1999 tornado. *21st Conf. on Severe Local Storms*, San Antonio, TX, Amer. Meteor. Soc.

Sandifer, J. B., 2005: Meteorological measurements with a MWR-05XP phased array radar. Naval Postgraduate School.

Schneebeli, M., Grazioli, J., and Berne, A., 2014: Improved Estimation of the Specific Differential Phase SHIFT Using a Compilation of Kalman Filter Ensembles, *IEEE T. Geosci. Remote Sens*., **52**, 5137-5149, doi:10.1109/TGRS.2013.2287017, 2014.

Shedd, L., M. R. Kumjian, I. Giammanco, T. Brown-Giammanco, and B. R. Maiden, 2021: Hailstone shapes. *J. Atmos. Sci.*, **78 (2),** 639–652, https://doi.org/10.1175/JAS-D-20-0250.1.

Snyder, J. C., A.V. Ryzhkov, H. B. Bluestein, and S. F. Blair, 2014: Polarimetric Analysis of Two Giant-Hail-Producing Supercells Observed by X-band and S-band Radars. *27th Conf. on Severe Local Storms,* Madison, WI. Amer. Meteor. Soc.

Snyder, J. C., H. B. Bluestein, V. Venkatesh, and S. J. Frasier, 2013: Observations of polarimetric signatures in supercells by an X-band mobile Doppler radar. *Monthly Weather Review*, **141 (1),** 3–29, https://doi.org/10.1175/MWR-D-12-00068.1.

Snyder, J. C., H. B. Bluestein, G. Zhang, and S. J. Frasier, 2010: Attenuation correction and hydrometeor classification of high-resolution, X-band, dual-polarized mobile radar measurements in severe convective storms. *J. Atmos. Oceanic Technol*., **27**, 1979-2001, https://doi.org/10.1175/2010JTECHA1356.1.

Stepanian, P. M., K. G. Horton, V. M. Melnikov, D. S. Zrnić, and S. A. Gauthreaux Jr., 2016: Dual-polarization radar products for biological applications. *Ecosphere*, **7**, e01539.

Straka, J. M., Zrnić, D. S., & Ryzhkov, A. V. 2000: Bulk hydrometeor classification and quantification using Polarimetric Radar Data: Synthesis of relations. *J. Appl. Meteor.,* **39(8),** 1341–1372.

Van Den Broeke, M. S. ,2015a: Polarimetric tornadic debris signature variability and debris fallout signatures. *J. Appl. Meteor*., **54(12**), 2389–2405. https://doi.org/10.1175/jamc-d-15-0077.1

Vivekanandan, J., Zrnic, D. S., Ellis, S. M., Oye, R., Ryzhkov, A. V., & Straka, J., 1999: Cloud Microphysics Retrieval Using S-Band Dual-Polarization Radar Measurements. *Bull. Amer. Meteor. Soc.*, **80(3),** 381-388.

Vulpiani. G., Montopoli, M., Passeri, L., Gioia, G., Giordano, P., & Marzano, F., 2012: On the Use of Dual-Polarized C-Band Radar for Operational Rainfall Retrieval in Mountainous Areas. *J. Appl. Meteor. Climatol*., **51**, 405-425, doi: 10.1175/JAMC-D-10-05024.1.

Wienhoff, Z. B., H. B. Bluestein, D. W. Reif, R. M. Wakimoto, L. J. Wicker, and J. M. Kurdzo, 2020: Analysis of debris signature characteristics and evolution in the 24 May 2016 Dodge City, Kansas, tornadoes. *Mon. Wea. Rev*., **148,** 5063–5086.

Witt, A., D. W. Burgess, A. Seimon, J. T. Allen, J. C. Snyder, and H. B. Bluestein, 2018: Rapid-scan radar observations of an Oklahoma tornadic hailstorm producing giant hail. *Weather and Forecasting*, **33 (5),** 1263–1282, https://doi.org/10.1175/ WAF-D-18-0003.1.

Wurman, J., D. Dowell, Y. Richardson, P. Markowski, E. Rasmussen, D. Burgess, L. Wicker, and H. Bluestein, 2012: The Second Verification of the Origins of Rotation in Tornadoes Experiment: VORTEX2. *Bull. Amer. Meteor. Soc*., **93**, 1147–1170.

Wurman, J., J. Straka, E. Rasmussen, M. Randall, and A. Zahrai, 1997: Design and deployment of a portable, pencil-beam, pulsed, 3-cm Doppler radar. *J. Atmos. Oceanic Technol*., **14**, 1502–1512.

Zrnic, D. S., G. Zhang, V. Melnikov, and J. Andric, 2010: Three-body scattering and hail size. *J. Appl. Meteor. Climatol*, **49 (4)**, 687–700, https://doi.org/10.1175/2009JAMC2300.1.

Zrnić, D., D. W. Burgess, and L. Hennington, 1985: Doppler spectra and estimated windspeed of a violent tornado. *J. Climate Appl. Meteor.,* **24,** 1068–1081.